HHS Public Access

Author manuscript

Cancer Discov. Author manuscript; available in PMC 2020 March 01.

Published in final edited form as:

Cancer Discov. 2019 September ; 9(9): 1248–1267. doi:10.1158/2159-8290.CD-19-0061.

Glioma Stem Cell Specific Super Enhancer Promotes Polyunsaturated Fatty Acid Synthesis to Support EGFR Signaling

Ryan C. Gimple[1,2], **Reilly L. Kidwell**[1], **Leo J.Y. Kim**[1,2], **Tengqian Sun**[3], **Anthony D. Gromovsky**[4], **Qiulian Wu**[1], **Megan Wolf**[5], **Deguan Lv**[1], **Shruti Bhargava**[1], **Li Jiang**[1], **Briana C. Prager**[1,2,6], **Xiuxing Wang**[1], **Qing Ye**[3], **Zhe Zhu**[1], **Guoxin Zhang**[1], **Zhen Dong**[1], **Linjie Zhao**[1], **Derrick Lee**[1], **Junfeng Bi**[7], **Andrew E. Sloan**[8,9], **Paul S. Mischel**[7,10,11], **J. Mark Brown**[4], **Hu Cang**[3], **Tao Huan**[5], **Stephen C. Mack**[12,13], **Qi Xie**[1,14,#], **Jeremy N. Rich**[1,15,#]

[1.]Division of Regenerative Medicine, Department of Medicine, University of California, San Diego, San Diego, CA, USA.

[2.]Department of Pathology, Case Western University, Cleveland, OH, USA.

[3.]Salk Institute for Biological Studies, La Jolla, CA, USA.

[4.]Department of Cellular and Molecular Medicine, Cleveland Clinic Lerner Research Institute, Cleveland, OH, USA.

[5.]Department of Chemistry, University of British Columbia, 2036 Main Mall, Vancouver, British Columbia, V6T 1Z1, Canada.

[6.]Cleveland Clinic Lerner College of Medicine of Case Western Reserve University, Cleveland, Ohio, USA.

[7.]Ludwig Institute for Cancer Research, University of California at San Diego, La Jolla, CA, USA.,UCSD School of Medicine, La Jolla, CA 92093, USA.

[8.]Case Comprehensive Cancer Center, Case Western Reserve University School of Medicine, Cleveland OH, 44106, USA.

[9.]Department of Neurological Surgery, University Hospitals–Cleveland Medical Center, Cleveland OH, 44106, USA.

[10.]Department of Pathology, UCSD School of Medicine, La Jolla, CA 92093, USA.

[#]**Corresponding Author Address:** Qi Xie. No.18, Shilongshan Road, Cloud Town, Xihu District, Hangzhou, Zhejiang Province, China, 310024. Phone: +8615501201789. (xieqi724@gmail.com)., Jeremy N. Rich. 3855 Health Sciences Drive, La Jolla, CA, 92093. Phone: 858-822-2703. (drjeremyrich@gmail.com).

AUTHOR CONTRIBUTIONS

Conceptualization: R.C.G., L.J.Y.K., Q.X., S.C.M., Q.X., J.N.R.
Methodology: R.C.G., R.L.K, Q.W., G.Z., Q.X., T.S., Q.Y., J.M.B., A.D.G.
Software: R.C.G., B.C.P., L.J.Y.K, S.C.M.
Investigation: R.C.G., R.L.K, S.B., D.L., D.L., L.J., L.Z., Z.Z., X.W., L.J.Y.K., G.Z., Q.X., T.H., A.D.G., Q.Y., Q.W.
Resources: Q.W., X.W., A.E.S., J.N.R.
Writing: R.C.G., R.L.K., A.D.G., J.M.B., J.N.R.
Visualization: R.C.G., R.L.K, L.J.Y.K., B.C.P., T.H.
Supervision: J.M.B., H.C., S.C.M., J.N.R.
Funding acquisition: J.N.R.

Conflict of Interest: The authors declare no potential conflicts of interest.

[11.]Moores Cancer Center, UCSD School of Medicine, La Jolla, CA 92093, USA.

[12.]Department of Pediatrics, Baylor College of Medicine, Houston, TX, USA.

[13.]Dan L. Duncan Cancer Center, Houston, TX, 77030, USA.

[14.]Institute of Basic Medical Sciences, Westlake Institute for Advanced Study, Westlake University, Hangzhou, China.

[15.]Department of Neurosciences, University of California, San Diego, School of Medicine, La Jolla, CA 92037, USA.

Abstract

Glioblastoma ranks among the most aggressive and lethal of all human cancers. Functionally defined glioma stem cells (GSCs) contribute to this poor prognosis by driving therapeutic resistance and maintenance of cellular heterogeneity. To understand the molecular processes essential for GSC maintenance and tumorigenicity, we interrogated the super-enhancer landscapes of primary glioblastoma specimens and *in vitro* GSCs. GSCs epigenetically upregulated ELOVL2, a key polyunsaturated fatty acid synthesis enzyme. Targeting ELOVL2 inhibited glioblastoma cell growth and tumor initiation. ELOVL2 depletion altered cellular membrane phospholipid composition, disrupted membrane structural properties, and diminished EGFR signaling through control of fatty acid elongation. In support of the translational potential of these findings, dual targeting of polyunsaturated fatty acid synthesis and EGFR signaling had a combinatorial cytotoxic effect on GSCs.

Keywords

ELOVL2; super-enhancer; fatty acid; glioblastoma; EGFR

INTRODUCTION

Glioblastoma is the most prevalent primary intrinsic brain tumor in adults, has a median survival of less than 15 months, and is universally lethal despite maximal therapy (1). Recent investigation of cancer stem cells, a subset of tumor cells proposed to sustain tumorigenesis and cellular heterogeneity (2), has contributed to an improved understanding of this deadly cancer. While there has been controversy surrounding the origins and defining molecular characteristics of cancer stem cells, functionally defined glioma stem cells (GSCs) promote glioblastoma pathogenesis and contribute to the suboptimal efficacy of current treatment options through mediating angiogenesis (3), resistance to radiotherapy (4) and chemotherapy (5), invasion into normal brain (6), and self-renewal (7). These characteristics implicate GSCs as important targets for the design of novel therapeutics for glioblastoma.

While glioblastoma and other cancers have traditionally been viewed as genetic diseases, epigenetic alterations play an important role in cancer pathogenesis and progression. In glioblastomas and other brain tumors, epigenome and chromatin regulators are frequently disrupted and promote malignant phenotypes (8,9). As therapeutics targeting genomic drivers have been, at best, marginally effective for glioblastoma, new therapeutic paradigms

that integrate the epigenetic state of GSCs may yield benefit. Super-enhancers, defined as regulatory regions with unusually strong enrichment for the binding of transcriptional coactivators, function as master epigenetic regulators that define cell state, regulate genes controlling cell identity, orchestrate cell-type dependent transcriptional networks, and are enriched for disease-associated genetic variation (10–12). We hypothesized that interrogation of super-enhancer profiles may provide insight into the cell-type-specific molecular processes that underlie GSC maintenance, identify cancer-dependency genes and genetic programs critical to glioma initiation and progression, and translate into new therapeutic strategies.

Cancer cells coopt aberrant metabolic networks to gain proliferative advantages through a number of avenues. In diffuse glioma, IDH1 and IDH2 mutations are critical tumor-initiating events that establish altered metabolic networks that drive widespread epigenetic reprogramming through establishment of a glioma CpG-island methylator phenotype (G-CIMP) (13,14). In other cancers, altered lipid metabolism and fatty acid synthesis are also important for metabolic reprogramming (15). Lipid composition is greatly altered in gliomas with enrichment for free fatty acids and polyunsaturated fatty acids (16). Cholesterol uptake, synthesis, and signaling features are key dependencies of GSCs and have been the targets of therapeutic development efforts (17–20). Aberrant EGFR and other receptor tyrosine kinase (RTK) signaling pathways, which are commonly dysregulated in glioma, drive a metabolic shift favoring fatty acid synthesis and a dependence on this enhanced lipogenesis (21–23). Thus, we utilized an unbiased cell-state dependent super-enhancer profiling approach to identify epigenetically driven oncogenes and investigated the underlying regulatory networks that drive expression of these genes and their role in GSC biology.

RESULTS

Discovery of stem-state dependent epigenetically upregulated genes

To identify GSC-specific super-enhancers in an unbiased manner, we utilized an *in silico* super-enhancer target selection strategy to identify super-enhancer associated genes present within glioblastoma surgical specimens that overlapped with stem state-specific enhancers (Figure 1A). We profiled the epigenetic landscape of 10 glioblastoma surgical resection samples and 15 normal brain samples through H3K27ac ChIP-seq (histone 3 lysine 27 acetylation chromatin immunoprecipitation followed by next-generation sequencing) datasets that we and others generated (19,24,25). Both typical enhancer and super-enhancer analyses revealed that samples clustered together based on disease status (Figures 1B–D), suggesting that glioblastoma specimens contained unique epigenetic landscapes that promote tumorigenesis. Annotation of super-enhancer regions to the nearest gene across 10 glioblastoma primary tissue samples identified a number of consistent targets, including EGFR, SOX2, CTDSP2, MIR9–1, and POU3F3 (Figure S1A). We focused on super-enhancers specific to glioblastoma compared to normal brain samples (Figure 1E). To identify super-enhancers with potential stem-state specificity, we compared the epigenetic landscape of three human patient-derived GSCs with three matched serum differentiated glioma cells (DGCs) through analysis of H3K27ac ChIP-seq data (26) (Figure 1F). This approach permitted identification of cell-state specific epigenetically upregulated gene

networks in identical genetic backgrounds. GSC-specific constituent enhancers of glioblastoma specific super-enhancers displayed enrichment for transcriptional motifs of OCT4, NR2E1, and several SOX family members, which are important in GSC biology (Figure 1G). 148 super-enhancer associated genes were identified using this method and were assigned a "GSC specificity score" based on (1) the number of gained H3K27ac peaks in the GSC samples compared to DGC samples and (2) the mRNA expression difference between GSC and DGC samples (Figure 1H). Neurogenesis, nervous system development pathways, and pathways involved in oligodendrocyte and cellular differentiation processes were enriched in these GSC-specific super-enhancer-associated genes (Figure 1I). To prioritize these genes for further study, we selected genes with (1) prognostic significance in The Cancer Genome Atlas (TCGA) database, where high gene expression was associated with poor glioblastoma patient survival in either IDH wildtype or IDH mutant glioblastomas (Figures S1B–D) and (2) elevated expression in glioblastoma tissue versus normal brain tissue from integrated analyses of the TCGA and GTEx databases (Figures 1J and S1E). Fewer genes carried prognostic significance when restricted to IDH wildtype glioblastomas (Figures S1C). The three top ranked genes (WSCD1, ELOVL2, and KLHDC8A) were selected for further validation and analyses (Figure 1K).

Super-enhancer associated target genes are functionally critical in GSCs

To validate the role of genes marked by super-enhancers in glioblastoma biology, we interrogated the roles of these relatively uncharacterized genes in GSC biology. WSCD1, ELOVL2, and KLHDC8A were each marked by a super-enhancer specific for glioblastoma and GSCs (Figures 2A–C), portended a negative prognosis in glioblastoma, and were overexpressed in glioblastoma surgical tissues compared with normal brain (Figures 2D–F). Each super-enhancer associated gene was upregulated in glioblastoma cells compared to other tumor cellular components, including astrocytes, oligodendrocytes, and immune cell fractions in single-cell RNA-sequencing (scRNAseq) datasets (27) (Figures 2G–I). In a validation panel of seven patient-derived GSCs, ELOVL2, KLHDC8A, and WSCD1 mRNA levels were increased in GSCs compared to their differentiated tumor counterparts (2J–L). Differentiation of DGCs was validated by detecting decreased mRNA levels of *SOX2* and *OLIG2* and increased mRNA levels of *GFAP* compared to GSCs (Figures S2A–C). These findings were verified using two independent biological replicates (Figures S2D–I). Defining the precise gene targets of super-enhancers remains an unresolved challenge. Several factors complicate this task: (1) enhancers can regulate more than a single gene, (2) chromosomal looping events can lead to enhancer-gene pairs that are distant in the linear DNA sequence, and (3) enhancers may function in a cell-type specific manner (28). Super-enhancers depend on the binding of transcriptional co-activators to drive downstream gene expression, including BRD4. Inhibition of BRD4 with JQ1 blocks transcriptional co-activation effects and specifically diminishes expression of super-enhancer driven genes (29,30). We treated three patient-derived GSCs with JQ1 and observed diminished mRNA levels of *ELOVL2* and *KLHDC8A*, along with a positive control gene (*MYC*) in three GSCs (Figures S2J–M), supporting ELOVL2 and KLHDC8A as driven by stem-cell specific super-enhancers. Knockdown of the super-enhancer-associated genes with two independent non-overlapping shRNAs per gene inhibited cell proliferation of two patient-derived GSCs (GSC387 and GSC3565) (Figures 2M–O and S2N–P). Collectively, these results confirm

that these super-enhancer-regulated genes are essential for GSC maintenance. We interrogated the role of ELOVL2 in GSC biology, as among the genes tested, ELOVL2 most robustly stratified patients based on prognosis, demonstrated responsiveness to JQ1, and may be amenable to therapeutic targeting due to its role as an enzyme.

Stem-state specific transcription factors contribute to regulation of ELOVL2 through a GSC-specific super-enhancer

To functionally dissect drivers of the putative ELOVL2 super-enhancer, we analyzed available GSC ChIP-seq data (26) and found that two essential neurodevelopmental and stem cell transcription factors, SOX2 and OLIG2, bound within a 500-bp region of the ELOVL2 super-enhancer in GSCs, overlapping with a region of open chromatin and characterized by a relative minimum in H3K27ac signal (Figure 3A). In clinical samples from TCGA, ELOVL2 expression positively correlated with expression of SOX2 and OLIG2 in the classical subtype of glioblastoma (Figure 3B), which is characterized by EGFR activity. In direct ChIP-PCR studies, SOX2 binding was enriched in three patient-derived GSCs at this locus compared to a negative control region (Figure 3C). Furthermore, knockdown of SOX2 with three independent non-overlapping shRNAs diminished expression of ELOVL2 (Figure 3D). To assess the functional regulatory role of this locus and the super-enhancer region, we recruited a transcriptional repressor complex (KRAB) to this non-coding region using a catalytically-dead CRISPR-Cas9 system (dCas9) (Figure 3E), which inhibited ELOVL2 expression at the mRNA level following recruitment of the dCas9-KRAB complex (Figure 3F). Silencing of the super-enhancer component contributed to a cell proliferation defect (Figure 3G) and decreased protein levels of ELOVL2 in GSCs to a level more consistent with that of a differentiated glioma cell (Figures 3H–J). Collectively, these findings indicate that this super-enhancer element drives expression of ELOVL2, with contributions from the stem-state specific transcription factor, SOX2.

ELOVL2 maintains GSCs

To generalize the contribution of ELOVL2 in GSCs, ELOVL2 knockdown in four additional patient-derived GSCs confirmed our previous findings of impaired cell proliferation capacity (Figures 4A and S3A–B). To address potential off-target effects associated with shRNAs, we generated an ELOVL2 knockout using CRISPR-Cas9 technology (Figures S3C–D), which led to a similar cell proliferation defect *in vitro* (Figure 4B). Two additional shRNAs targeting non-overlapping sequences in the ELOVL2 transcript also impaired cell proliferation (Figures S3E–F). Extreme limiting dilution assays (ELDA) are a surrogate for cellular self-renewal capacity. Using an *in vitro* ELDA, GSC stem cell frequency and self-renewal were diminished following depletion of ELOVL2 in two patient-derived GSCs (Figures 4C and S3G). ELOVL2 knockdown induced apoptotic cell death in two GSCs, as measured by annexin V staining (Figure 4D) and decreased in expression of GSC markers (SOX2 and OLIG2), further supporting a role in the loss of stemness (Figure S3H). ELOVL2 knockdown induced cell cycle defects, including accumulation of cells in sub-G_0 and G_1 phases (Figure S3I). To address the cell-state dependency for ELOVL2 expression, ELOVL2 was depleted by shRNAs in three patient-derived GSCs following *in vitro* differentiation, revealing no significant changes in cell proliferation capacity in the differentiated glioma cells (Figures 4E–G and S3J). While GSCs underwent apoptosis as

indicated by cleaved PARP, matched DGCs display only the uncleaved protein (Figures 4H – J). Next, we interrogated the potential functional roles of ELOVL2 in non-neoplastic cells. Knockdown of ELOVL2 impaired proliferation of three neural stem cells (Figure S4A), but had minimal impact on non-neoplastic neural cells derived from epilepsy tissue resection specimens (Figure S4B). To further understand the dependency on ELOVL2 across numerous cancer cell types, we interrogated the Cancer Dependency Map (www.depmap.org). Across a panel of 558 cell lines profiled using whole genome CRISPR-Cas9 screening and 711 cell lines profiled using whole genome shRNA screening, ELOVL2 was not a pan-essential gene (Figures S4C and S4D). In normal brain profiled by scRNA-seq (31), ELOVL2 colocalizes with SOX2 and is enriched in radial glial and intermediate progenitor cell populations, indicating a possible role in maintenance of stemness (Figures S4E–H). Thus, ELOVL2 is critical for the maintenance of GSCs, but is not essential for DGCs or more differentiated non-neoplastic neural cells.

Glioblastoma stem cells depend on polyunsaturated fatty acid synthesis for maintenance of membrane phospholipid composition and integrity

ELOVL2 is an endoplasmic reticulum transmembrane protein that functions in the synthesis of long chain ω3 and ω6 polyunsaturated fatty acids (LC-PUFAs). ELOVL2 converts arachidonic acid (ω6-C20:4 AA) and eicosapentaenoic acid (ω3-C20:5 EPA) to the longer chain PUFAs docosapentaenoic acid (ω6-C22:5 DPA) and docosahexaenoic acid (ω3-C22:6 DHA). Mass spectrometry analysis of total fatty acid levels revealed elevated LC-PUFAs (ω3-DHA and ω6-DPA) in GSCs compared to matched DGCs, suggesting that increased expression of ELOVL2 in GSCs drives elongation to form these intermediate species (Figures 5A and 5B). We hypothesized that this metabolic network producing LC-PUFAs is upregulated in GSCs and that disruption impairs GSC viability. In accordance with this model, supplementation of cell culture media with the LC-PUFAs ω3-DHA or ω6-DPA partially rescued the cell proliferation defect caused by ELOVL2 knockdown (Figures S5A and S5B), indicating LC-PUFA deficiency caused by ELOVL2 knockdown contributes to the observed phenotypes. LC-PUFAs play a number of roles including serving as an energy source, acting as a key component of membrane phospholipids, and mediating intracellular signaling via the NFκB, PPAR, and SREBP networks. In addition to nuclear signaling roles, LC-PUFAs are important as a reservoir for eicosanoid production – via oxygenation by COX, LOX, and CYP systems. To further narrow the role of ELOVL2 in GSCs, we performed global mass spectrometry-based metabolomic analysis following ELOVL2 knockdown and identified differential metabolites in two patient-derived GSCs in both positive and negative modes (Figures S5C–F). Several metabolites were consistently altered following ELOVL2 knockdown (Figures 5C and 5D), with enrichment in phosphatidylserine species (Figure 5E). Pathway analyses of differential metabolites within each GSC demonstrated a consistent enrichment for purine salvage and pyrimidine degradation pathways in GSCs with an associated increase in the purine salvage products, hypoxanthine and guanine (Figures S5G–J).

As the most consistent trends suggested alterations in phospholipid metabolism, we utilized a mass spectrometry-based shotgun lipidomics approach to gain a more comprehensive view of lipid alterations following ELOVL2 knockdown, revealing (1) an increase in the

quantities of phospholipids, including a number of phosphatidylcholine and phosphatidylethanolamine species, and (2) a reciprocal decrease in several lysophospholipids, including lysophosphoethanolamines (Figures 5F and 5G). ELOVL2 knockdown contributed to alteration in transcriptional signatures associated with phospholipid remodeling and phospholipase activity (Figures 5H and S5K). These findings suggest alterations in the Lands' cycle – a series of phospholipase-driven deacylation and lysophospholipid acyltransferase-driven reacylation reactions that synergize to alter phospholipid composition and control membrane asymmetry, diversity, and fluidity. As ELOVL2 knockdown contributed to an altered cellular phospholipid profile, we hypothesized that this change could impair cell membrane structure. Fluorescence Recovery After Photobleaching (FRAP) assays of cellular membranes showed that ELOVL2 knockdown impaired fluorescence recovery in GSCs, indicating a decrease in cellular membrane fluidity (Figures 5I–K). Thus, ELOVL2 promotes cellular membrane composition and architecture in GSCs.

Polyunsaturated fatty acid synthesis supports efficient EGFR signaling

To understand the functional consequences of ELOVL2 depletion and its associated signaling networks, we interrogated the TCGA dataset by correlating ELOVL2 mRNA levels to potential downstream signaling proteins measured by reverse phase protein array (RPPA) in surgical biopsy glioblastoma tissues. This revealed high expression of ELOVL2 strongly associated with key receptor tyrosine kinase signaling elements, including EGFR and activated, phosphorylated EGFR (pY1068 and pY1173) (Figures 6A and 6B). Upon segregation of the TCGA dataset based on ELOVL2 expression, EGFR mRNA was one of the most differentially expressed genes (Figure S6A). Reciprocally, ELOVL2 was one of the most differentially expressed genes following segregation based on EGFR expression status (Figure S6B). ELOVL2 mRNA expression is elevated in the classical glioblastoma subtype, which is characterized by EGFR amplification and is defined, in part, through ELOVL2 expression (Figure S6C). Across multiple patient datasets, ELOVL2 and EGFR mRNA levels were highly correlated (Figure S6D). RNA-sequencing analysis following ELOVL2 knockdown in two patient-derived GSCs revealed altered expression in gene sets associated with cell cycle progression and MAPK regulation, an important pro-tumorigenic cascade linked to EGFR signaling (Figures 6C and S6E–F). To assess the effects of ELOVL2 knockdown on EGFR signaling, we analyzed EGFR expression at the mRNA and protein levels. While mRNA levels of EGFR were not affected or even increased in several GSCs (Figure 6D), knockdown of ELOVL2 decreased the levels of total EGFR protein, activated phosphorylated EGFR, and activated ERK (a downstream EGFR signaling element) in two GSCs (Figure 6E), suggesting ELOVL2 regulates EGFR post-transcriptionally. These findings were further validated by targeting the ELOVL2 super-enhancer using the dCas9-KRAB repression approach, indicating the ELOVL2 super-enhancer supports EGFR signaling (Figure 6F).

To assess the role of LC-PUFAs in EGFR signaling, cell culture media were supplemented with the LC-PUFA ELOVL2 products, ω3-DHA and ω6-DPA, which induced EGFR signaling with increased phosphorylation of EGFR and activation of downstream ERK signaling (Figure 6G). This effect was only observed 24 and 48 hours following addition of

LC-PUFAs, suggesting that the fatty acids do not directly stimulate EGFR signaling elements, but rather must be metabolized first. These findings, together with our observations that ELOVL2 regulates EGFR signaling through a post-transcriptional mechanism and that ELOVL2 affects membrane phospholipid metabolism, prompted us to investigate the dynamics of EGFR membrane localization. EGFR stability and signaling are regulated through interactions with cellular membranes (32,33). Using super-resolution stochastic optical reconstruction microscopy (STORM) (Figures 6H and S6G) and flow cytometry (Figures 6I and S6H), EGFR membrane localization and intensity decreased upon ELOVL2 knockdown. Targeting the ELOVL2 super-enhancer element similarly reduced the sharp membrane localization and intensity of EGFR as visualized by immunofluorescence (Figure 6J). LC-PUFA supplementation partially rescued EGFR phosphorylation following ELOVL2 knockdown, moderately enhanced ERK phosphorylation, and partially reduced PARP cleavage (Figure 6K). These data suggest that ELOVL2 acts through regulation of membrane phospholipid dynamics in GSCs and supports efficient EGFR signaling.

Because many cellular processes are affected by cell membrane integrity, we investigated the potential for ELOVL2 to impact other receptor tyrosine kinases (RTKs) beyond EGFR. In the TCGA, ELOVL2 mRNA levels were correlated with protein levels of EGFR, but were not correlated with other RTKs including IGF1R, MET, and KIT (Figure S6I). ELOVL2 knockdown by shRNA or the dCas9-KRAB super-enhancer targeting system reduced protein abundance of several RTKs including HER2/ERBB2, PDGFRβ, FGFR1, and INSR, while levels of IGF1Rβ and DDR1 were relatively unchanged (Figures S6J–L). We utilized rescue approaches to determine the contributions of signaling elements downstream of ELOVL2. Overexpression of EGFR rescued the cell proliferation defects caused by ELOVL2 knockdown (Figures 6L and 6M). Likewise, overexpression of a constitutive active form of MEK1 (S218D, S222D), which lies downstream of EGFR, partially rescued the ELOVL2-induced proliferation defect (Figures 6N, 6O and S6M). Treatment of GSCs with the known ERK activator lysophosphatidylethanolamine (LPE) partially rescued the ELOVL2-knockdown associated cell proliferation defect, suggesting that inhibition of downstream EGFR signaling nodes contributes to the ELOVL2 knockdown phenotypes (Figure S6N). We further interrogated the localization of EGFR at a single-cell level. Quantification of EGFR density across the cell using STORM imaging revealed that ELOVL2 knockdown abolished the preferential localization of EGFR along the periphery of the cell in the cell membrane in two GSCs (Figures S7A–F). Collectively, these findings indicate that ELOVL2 maintains efficient EGFR signaling in GSCs through its LC-PUFA products.

Polyunsaturated fatty acid synthesis is a viable clinical target for glioblastoma therapy

To determine the clinical relevance of the LC-PUFA synthesis pathway, we interrogated a study of metabolite profiling in cancer tissues (34). World Health Organization (WHO) grade IV glioma tissues contained greater quantities of the direct products of ELOVL2, including adrenic acid, ω6-docosapentaenoic acid and ω3-docosapentaenoic acid than WHO grade II gliomas (Figure 7A). Lipid metabolism gene signatures, including those related to phospholipid biosynthesis and remodeling, were associated with poor clinical outcomes in the TCGA dataset (Figures 7B and S8A–C). While no small molecules exist to specifically target ELOVL2, a small molecule inhibitor of FADS2 (SC-26196) has been utilized *in vitro*

and *in vivo* (35–37), although never in orthotopic glioblastoma models. FADS2 acts as a Δ−6 desaturase that catalyzes the enzymatic step immediately following ELOVL2 in the LC-PUFA synthesis cascade (Figure 7C). We hypothesized that FADS2 would serve essential functions in GSCs, which depend on ELOVL2-mediated LC-PUFA synthesis. FADS2 was upregulated in glioblastoma tissue as compared with normal brain tissue, was epigenetically upregulated in GSCs as compared with DGCs, and was upregulated at the mRNA level in nine patient-derived GSCs compared with matched DGCs (Figures 7D and S8D–E). Depletion of FADS2 with three independent, non-overlapping shRNAs greatly diminished cell proliferation capacity in two patient-derived GSCs, demonstrating its important functional role (Figure 7E). Knockdown of FADS2 phenocopied ELOVL2 knockdown, as demonstrated by induction of apoptosis and depletion of EGFR activity and downstream signaling elements upon knockdown (Figure 7F). In three GSCs, inhibition of FADS2 with SC-26196 impaired cell proliferation in a concentration-dependent manner, indicating that LC-PUFA synthesis enzymes play critical roles and can be targeted in glioblastoma (Figure 7G).

The connection between LC-PUFA synthesis networks and EGFR signaling efficacy suggests that dual targeting of these nodes would impair cell proliferation in a combinatorial manner. Treatment of GSCs with varying concentrations of the EGFR inhibitor, lapatinib, and the FADS2 inhibitor, SC-26196, showed that combinatorial treatment attenuated cell proliferation to a greater extent than either compound alone (Figures S8F). This interaction was synergistic in four patient-derived GSCs, with ZIP synergy scores ranging from 4.5 to 43 (for which scores greater than 1 indicate a synergistic interaction) (Figures 7H). The addition of SC-26196 to lapatinib further diminished EGFR phosphorylation and dampened ERK activation compared to lapatinib treatment alone, suggesting that SC-26196 may blunt compensatory signaling in response to lapatinib (Figure S8G). To explore the potential for ELOVL2 expression to predict sensitivity to EGFR inhibition in a pan-cancer setting, we queried the Cancer Therapeutics Response Portal, which contains data on 481 compounds tested across 860 cancer cell lines (38,39). Low mRNA levels of ELOVL2 were associated with increased sensitivity to a variety of EGFR inhibitors, including afatinib, erlotinib, and lapatinib (Figure S8H). This is consistent with our finding that targeting LC-PUFA metabolism sensitizes GSCs to EGFR inhibition. The combination of SC-26196 and lapatinib did not display synergy in astrocytes or non-malignant neural cells, suggesting specific effects in GSCs (Figure S8I).

Finally, we interrogated the potential for therapeutic targeting of LC-PUFA synthesis in an *in vivo* setting. Mice bearing orthotopic xenografts derived from patient-derived GSCs transduced with one of two independent shRNAs targeting ELOVL2 displayed a prolonged time to onset of neurological signs compared to mice bearing GSCs transduced with a non-targeting shRNA control (shCONT), indicating that ELOVL2 knockdown impaired *in vivo* tumor formation capacity (Figures 7I and S8J). Histological images from tumor-bearing brains show increased *in vivo* growth of tumors derived from GSCs transduced with shCONT, whereas tumors derived from GSCs transduced with either of two shRNAs targeting ELOVL2 were greatly reduced (Figures 7I and S8J). To address the potential for therapeutic targeting of ELOVL2 and LC-PUFA synthesis for glioblastoma, we utilized three approaches. As pharmacologic ELOVL2 inhibitors are not currently available, we

genetically targeted ELOVL2 then interrogated the additional benefit of lapatinib. Survival of mice bearing xenografts derived from cells with shRNAs targeting ELOVL2 was further prolonged with lapatinib treatment (Figure S8K). Due to concerns regarding systemic toxicities and drug delivery, we treated GSCs prior to implantation into the brains of NSG mice. Combinatorial treatment of GSCs *in vitro* with SC-26196 and lapatinib extended the latency to tumor formation compared to vehicle control or single agent therapies (Figure 7J). Finally, we assessed the efficacy of the small molecule FADS2 inhibitor, SC-26196, to impair tumor growth in a preclinical setting in combination with lapatinib. Intracranial tumors were generated by implantation of patient-derived GSCs into the brains of mice. Seven days after implantation, daily treatment with 125 mg/kg of SC-26196 and/or 30 mg/kg of lapatinib was initiated. Each agent alone prolonged survival of mice bearing orthotopic xenografts (Figure 7K). Treatment with a combination of the two agents prolonged survival compared to vehicle control, but induced additional toxicity, with hair thinning and weight loss (data not shown), with a non-statistical trend toward improvement in survival over the monotherapies (Figure 7K and S8L). This suggests that careful modulation of drug dosages may allow for a combinatorial benefit while minimizing toxicities and provides a rationale to develop novel selective pharmacologic inhibitors for ELOVL2 and LC-PUFA synthesis enzymes. Collectively, these results suggest that LC-PUFA synthesis pathways represent a potential therapeutic target for future drug development.

DISCUSSION

Using a super-enhancer profiling strategy, we now show that glioblastomas and GSCs epigenetically upregulate expression of ELOVL2 through activation of a non-coding regulatory region that is specific to GSCs. Super-enhancers drive genes essential for cancer cell survival in a number of cancer types, including in diffuse large B cell lymphoma (29), T-cell acute lymphoblastic leukemia (40), and medulloblastoma (41), among others (10,11). Our identification of ELOVL2 as a GSC-specific super-enhancer associated gene implicates the LC-PUFA synthesis network as a critical metabolic dependency in glioblastoma.

Fatty acids play a number of important roles in all cell types, including structural roles as components of the cell membrane in the form of phospholipids and cardiolipins. They also are components of key lipid signaling molecules, such as diacylglycerols (DAG), phosphotidylinositols (PIP family compounds), prostaglandins, leukotrienes, lysophosphatidic acid, and regulators of Wnt-βcatenin signaling through acylation (42). In addition to the numerous well-documented instances of metabolic derangements present in tumor cells, fatty acid metabolism is significantly altered in many cancer types (15). The key fatty acid synthesis enzyme, fatty acid synthase (FAS), is upregulated in many human cancers (15) including breast cancer, prostate cancer, colon cancer, ovarian cancer, and glioma (43), among others, and is frequently associated with poor patient prognosis. While normal tissues mainly rely on exogenous fatty acids for energetic and structural needs, cancer cells depend on endogenous fatty acid synthesis for nearly all of their production of membrane phospholipids and energetic needs (44,45) and frequently use alternative fuels (46).

The metabolic enzymes implicated in our study, ELOVL2 and FADS2, elongate and desaturate LC-PUFAs, respectively. It has been known for decades that glioblastoma tissues contain higher free fatty acid, LC-PUFAs, and altered phospholipid composition as compared to normal brain tissue (16,47). However, the precise roles for these fatty acids are more complex. In ovarian cancer, unsaturated fatty acids were found to be enriched in cancer stem cells with inhibition of fatty acid desaturases resulting in impaired tumor initiation capacity (48). Other reports have indicated that LC-PUFAs are cytotoxic to glioblastoma cells (49). It is likely that the effects of these fatty acids are both context- and concentration-dependent. One major role for fatty acid synthesis in glioblastoma is the connection between oncogenic signaling pathways and reprogramming of cellular metabolism. mTOR signaling has been shown to upregulate *de novo* fatty acid synthesis to promote hepatocellular carcinoma progression (50). EGFR signaling in glioblastoma upregulates SREBP1, a key transcription factor that drives expression of lipogenic genes, and this relationship establishes a synthetic lethality between activated EGFR and lipid metabolism enzymes (17,18,21,22). Our results complement and build on this model by suggesting a positive feedback loop whereby LC-PUFA synthesis supports efficient EGFR signaling through preservation of cellular membrane structure. Other studies have linked fatty acid metabolites, including prostaglandin E2 and leukotrienes, as regulators of EGFR signaling (51,52) and fatty acid metabolites may potentiate EGFR signaling through post-translational modifications (53). As the most commonly amplified oncogene in glioblastoma, EGFR has served as a target for numerous preclinical and clinical trials for the treatment of glioblastoma. However, EGFR-targeting agents have invariably failed to extend patient survival. Our data suggest that combinatorial approaches targeting both EGFR signaling elements as well as LC-PUFA synthesis may enhance therapeutic efficacy. In summary, we utilized a super-enhancer screening approach that implicated ELOVL2 as a critical epigenetically-driven dependency in glioblastoma. ELOVL2 promotes LC-PUFA synthesis, which is essential for the maintenance of cellular membrane architecture and which supports efficient EGFR signaling (Figure S8M). In conclusion, our results suggest that aberrant chromatin regulation in cancer can drive oncogenic signal transduction through dysregulation of metabolic pathways that contribute to membrane dynamics, offering novel combinatorial strategies for lethal cancers.

METHODS

CONTACT FOR REAGENT AND RESOURCE SHARING

Further information and requests for resources and reagents should be directed to and will be fulfilled by the corresponding author, Dr. Jeremy N. Rich (drjeremyrich@gmail.com).

EXPERIMENTAL MODELS AND SUBJECT DETAILS

GSC derivation—Glioblastoma tissues were obtained from excess surgical resection samples from patients at Duke University or Case Western Reserve University after review by neuropathology with appropriate consent and in accordance with an IRB-approved protocol (090401). All patient studies were conducted in accordance with the Declaration of Helsinki. GSC387 and GSC3565 were derived by our laboratory and transferred via a material transfer agreement from Duke University. MGG4, MGG6, and MGG8 were a kind

gift of Hiroaki Wakimoto and obtained via a material transfer agreement from Massachusetts General Hospital. GSC2012, GSC1919, GSC-CW738, GSC1517, GSC3264, GSC3028, and GSC3136 were derived by our laboratory as previously reported. GSC23 was transferred via a material transfer agreement from MD Anderson Cancer Center. All GSCs were cultured in Neurobasal media (Invitrogen) supplemented with B27 without vitamin A (Invitrogen), EGF, and bFGF (20 ng/ml each; R&D Systems), sodium pyruvate, and glutamax. To decrease the incidence of cell culture-based artifacts, patient-derived xenografts were produced and propagated as a renewable source of tumor cells for study. Short Tandem Repeat (STR) analyses were performed to authenticate the identity of each tumor model used in this article on a yearly basis. Cells were stored at −160°C when not being actively cultured. Mycoplasma testing was performed by qPCR cellular supernatants on a yearly basis. Cells were grown for fewer than 20 *in vitro* passages from xenografts.

Other cell models—The non-malignant neural stem cell models ENSA, hNP1, and NSC11 were used in this study. ENSA (ENS-tem-A) is a human embryonic stem derived neural progenitor cell (Millipore Sigma, Cat SCC003). NSC11 is a human induced pluripotent derived neural progenitor cell (Alstem, Cat # hNSC11). hNP1 (STEMEZ hNP1) is a human neural progenitor cell (Neuromics, Cat # HN60001). The non-malignant neural cells (NM53, NM55, NM176, and NM263) were derived from excess surgical resection tissue from patients undergoing surgery for epilepsy. Human astrocyte #1 was obtained from Fisher Scientific/Gibco (Cat # N7805200). Human astrocyte #2 was obtained from ScienCell (Cat #1800).

In vivo tumorigenesis—For ELOVL2 shRNA experiments, intracranial xenografts were generated by implanting 10,000 human-derived GSCs into the right cerebral cortex of NSG mice (NOD.Cg-Prkdcscid Il2rgtm1Wjl/SzJ, The Jackson Laboratory, Bar Harbor, ME, USA) at a depth of 3.5 mm under a University of California, San Diego Institutional Animal Care and Use Committee (IACUC) approved protocol.

For *in vivo* drug combination studies, intracranial xenografts were generated by implanting 1,000 patient-derived GSCs (GSC387) into the right cerebral cortex of NSG mice as described above. Mice recovered for 7 days and were then treated daily with vehicle (0.5% methylcellulose), 125 mg/kg SC-26916, 30 mg/kg lapatinib, or a pre-mixed combination of 125 mg/kg SC-26916 and 30 mg/kg lapatinib by oral gavage.

For experiments investigating the effects of lapatinib treatment in mice implanted with shRNA knockdown cells, intracranial xenografts were generated by implanting 1,000 patient-derived GSCs (GSC387) transduced with either an shRNA targeting ELOVL2 (shELOVL2.308) or a non-targeting shRNA control into the right cerebral cortex of NSG mice as described above. Mice recovered for 7 days and were then treated daily with either vehicle (0.5% methylcellulose), 20 mg/kg Lapatinib, or 40 mg/kg Lapatinib by oral gavage.

For experiments interrogating the effects of combinatorial treatment on *in vivo* tumor formation capacity, GSCs (GSC387) were cultured *in vitro* and treated with either vehicle (DMSO), 10 μM SC-26916, 5 μM Lapatinib, or a combination of 10 μM SC-26916 and 5 μM Lapatinib for two days prior to implantation. Intracranial xenografts were generated by

implanting 5,000 cells from one of the four conditions into the right cerebral cortex of NSG mice as described above.

All murine experiments were performed under an animal protocol approved by the University of California, San Diego Institutional Animal Care and Use Committee. Healthy, wild-type male or female mice of NSG background, 4–6 weeks old, were randomly selected and used in this study for intracranial injection. Mice had not undergone prior treatment or procedures. Mice were maintained in 14 hours light/10 hours dark cycle by animal husbandry staff with no more than 5 mice per cage. Experimental animals were housed together. Housing conditions and animal status were supervised by a veterinarian. Animals were monitored until neurological signs were observed, at which point they were sacrificed. Neurological signs or signs of morbidity included hunched posture, gait changes, lethargy and weigh loss. Brains were harvested and fixed in 4% formaldehyde for 48 hours, stored at 4°C in 70% ethanol, and sectioned. Hematoxylin and eosin (H&E) staining was performed on sections for histological analysis.

For complete experimental details, see Supplementary Sections 1 and 2.

QUANTIFICATION AND STATISTICAL ANALYSES

All statistical analyses are described in the figure legends. For TCGA glioblastoma vs normal brain RNAseq calculations, Four-way ANOVA controlling for sex, age, and ethnicity with Benjamini and Hochberg false discovery rate (FDR) method was used for statistical analysis. For survival analyses, the Cox proportional hazards and log-rank analyses were used. For qPCR analyses, Student t-test was used to assess statistical significance, when appropriate. two-way repeated measures ANOVA was used for statistical analysis with Dunnett's multiple hypothesis test correction. For proliferation assays, two-way repeated measures ANOVA was used for statistical analysis with Dunnett's multiple hypothesis test correction.

DATA AND SOFTWARE AVAILABILITY

All newly generated raw sequencing data related to this study (related to ELOVL2 knockdown RNA sequencing) is available on GEO through the accession number: GSE130648. All data accessed from external sources and prior publications have been referenced in the text and corresponding figure legends. Additional data will be made available upon request.

Supplementary Material

Refer to Web version on PubMed Central for supplementary material.

ACKNOWLEDGEMENTS

This work was supported by grants provided by NIH. CA217065 (R.C.G); CA203101 (L.J.Y.K); CA217066 (B.C.P.); CA197718, CA154130, CA169117, CA171652, NS087913, NS089272, NS103434 (J.N.R) ; R01 HL122283, P50 AA024333, 4UL1TR000439, P30 CA043703, VeloSano Foundation (J.M.B.); CPRIT award, ALSF young investigator award, Rally research grant, BEAR Necessities Pediatric Cancer Foundation Grant, Children's Cancer Research Fund award, and Baylor College of Medicine Junior Faculty Award (S.C.M). NS073831 (P.S.M); National Institutes of Health (NIH) New Innovator Award 1-DP2-EB020400 (H.C.). A.E.S:

A217956–01, CA187780, NS 089272 as well as the Coulter, Ferry Foundation, Kimble and Gerald Kaufman Jr. Foundations and the Peter D. Cristal Chair at University Hospitals. This study was partially supported by University of British Columbia Start-up Grant awarded to Tao Huan. We thank the National Institute of Mental Health Chemical Synthesis and Drug Supply Program for providing us with the SC-26196 drug. We thank Chengwei He, PhD for assistance in developing *in vivo* treatment protocols with SC-26196. We thank Renliang Zhang, PhD for assistance in total fatty acid quantification. Figure S8M was prepared in part using images from Servier Medical Art by Servier (https://smart.servier.com/), which is licensed under a Creative Commons Attribution 3.0 Unported License (https://creativecommons.org/licenses/by/3.0/).

Financial Support: Listed in acknowledgements

REFERENCES

1. Ostrom QT, Gittleman H, Fulop J, Liu M, Blanda R, Kromer C, et al. CBTRUS Statistical Report: Primary Brain and Central Nervous System Tumors Diagnosed in the United States in 2008–2012. Neuro Oncol 2015;17 Suppl 4:iv1–iv62 doi 10.1093/neuonc/nov189. [PubMed: 26511214]
2. Reya T, Morrison SJ, Clarke MF, Weissman IL. Stem cells, cancer, and cancer stem cells. Nature 2001;414(6859):105–11 doi 10.1038/35102167. [PubMed: 11689955]
3. Bao S, Wu Q, Sathornsumetee S, Hao Y, Li Z, Hjelmeland AB, et al. Stem cell-like glioma cells promote tumor angiogenesis through vascular endothelial growth factor. Cancer research 2006;66(16):7843–8 doi 10.1158/0008-5472.CAN-06-1010. [PubMed: 16912155]
4. Bao S, Wu Q, McLendon RE, Hao Y, Shi Q, Hjelmeland AB, et al. Glioma stem cells promote radioresistance by preferential activation of the DNA damage response. Nature 2006;444(7120): 756–60 doi 10.1038/nature05236. [PubMed: 17051156]
5. Chen J, Li Y, Yu TS, McKay RM, Burns DK, Kernie SG, et al. A restricted cell population propagates glioblastoma growth after chemotherapy. Nature 2012;488(7412):522–6 doi 10.1038/nature11287. [PubMed: 22854781]
6. Wakimoto H, Kesari S, Farrell CJ, Curry WT Jr., Zaupa C, Aghi M, et al. Human glioblastoma-derived cancer stem cells: establishment of invasive glioma models and treatment with oncolytic herpes simplex virus vectors. Cancer research 2009;69(8):3472–81 doi 10.1158/0008-5472.CAN-08-3886. [PubMed: 19351838]
7. Singh SK, Hawkins C, Clarke ID, Squire JA, Bayani J, Hide T, et al. Identification of human brain tumour initiating cells. Nature 2004;432(7015):396–401 doi 10.1038/nature03128. [PubMed: 15549107]
8. Mack SC, Hubert CG, Miller TE, Taylor MD, Rich JN. An epigenetic gateway to brain tumor cell identity. Nat Neurosci 2016;19(1):10–9 doi 10.1038/nn.4190. [PubMed: 26713744]
9. Ceccarelli M, Barthel FP, Malta TM, Sabedot TS, Salama SR, Murray BA, et al. Molecular Profiling Reveals Biologically Discrete Subsets and Pathways of Progression in Diffuse Glioma. Cell 2016;164(3):550–63 doi 10.1016/j.cell.2015.12.028. [PubMed: 26824661]
10. Hnisz D, Abraham BJ, Lee TI, Lau A, Saint-Andre V, Sigova AA, et al. Super-enhancers in the control of cell identity and disease. Cell 2013;155(4):934–47 doi 10.1016/j.cell.2013.09.053. [PubMed: 24119843]
11. Hnisz D, Schuijers J, Lin CY, Weintraub AS, Abraham BJ, Lee TI, et al. Convergence of developmental and oncogenic signaling pathways at transcriptional super-enhancers. Mol Cell 2015;58(2):362–70 doi 10.1016/j.molcel.2015.02.014. [PubMed: 25801169]
12. Whyte WA, Orlando DA, Hnisz D, Abraham BJ, Lin CY, Kagey MH, et al. Master transcription factors and mediator establish super-enhancers at key cell identity genes. Cell 2013;153(2):307–19 doi 10.1016/j.cell.2013.03.035. [PubMed: 23582322]
13. Yan H, Parsons DW, Jin G, McLendon R, Rasheed BA, Yuan W, et al. IDH1 and IDH2 mutations in gliomas. N Engl J Med 2009;360(8):765–73 doi 10.1056/NEJMoa0808710. [PubMed: 19228619]
14. Turcan S, Rohle D, Goenka A, Walsh LA, Fang F, Yilmaz E, et al. IDH1 mutation is sufficient to establish the glioma hypermethylator phenotype. Nature 2012;483(7390):479–83 doi 10.1038/nature10866. [PubMed: 22343889]
15. Menendez JA, Lupu R. Fatty acid synthase and the lipogenic phenotype in cancer pathogenesis. Nature reviews Cancer 2007;7(10):763–77 doi 10.1038/nrc2222. [PubMed: 17882277]

16. Gopal K, Grossi E, Paoletti P, Usardi M. Lipid Composition of Human Intracranial Tumors: A Biochemical Study. Acta neurochirurgica 1963;11:333–47. [PubMed: 14064798]
17. Villa GR, Hulce JJ, Zanca C, Bi J, Ikegami S, Cahill GL, et al. An LXR-Cholesterol Axis Creates a Metabolic Co-Dependency for Brain Cancers. Cancer Cell 2016;30(5):683–93 doi 10.1016/j.ccell.2016.09.008. [PubMed: 27746144]
18. Cheng C, Ru P, Geng F, Liu J, Yoo JY, Wu X, et al. Glucose-Mediated N-glycosylation of SCAP Is Essential for SREBP-1 Activation and Tumor Growth. Cancer Cell 2015;28(5):569–81 doi 10.1016/j.ccell.2015.09.021. [PubMed: 26555173]
19. Wang X, Huang Z, Wu Q, Prager BC, Mack SC, Yang K, et al. MYC-regulated Mevalonate Metabolism Maintains Brain Tumor Initiating Cells. Cancer research 2017 doi 10.1158/0008-5472.CAN-17-0114.
20. Hale JS, Otvos B, Sinyuk M, Alvarado AG, Hitomi M, Stoltz K, et al. Cancer stem cell-specific scavenger receptor 36 drives glioblastoma progression. Stem cells 2014;32(7):1746–58 doi 10.1002/stem.1716. [PubMed: 24737733]
21. Guo D, Prins RM, Dang J, Kuga D, Iwanami A, Soto H, et al. EGFR signaling through an Akt-SREBP-1-dependent, rapamycin-resistant pathway sensitizes glioblastomas to antilipogenic therapy. Science signaling 2009;2(101):ra82 doi 10.1126/scisignal.2000446. [PubMed: 20009104]
22. Guo D, Reinitz F, Youssef M, Hong C, Nathanson D, Akhavan D, et al. An LXR agonist promotes glioblastoma cell death through inhibition of an EGFR/AKT/SREBP-1/LDLR-dependent pathway. Cancer discovery 2011;1(5):442–56 doi 10.1158/2159-8290.CD-11-0102. [PubMed: 22059152]
23. Guo D, Hildebrandt IJ, Prins RM, Soto H, Mazzotta MM, Dang J, et al. The AMPK agonist AICAR inhibits the growth of EGFRvIII-expressing glioblastomas by inhibiting lipogenesis. Proc Natl Acad Sci U S A 2009;106(31):12932–7 doi 10.1073/pnas.0906606106. [PubMed: 19625624]
24. Liu F, Hon GC, Villa GR, Turner KM, Ikegami S, Yang H, et al. EGFR Mutation Promotes Glioblastoma through Epigenome and Transcription Factor Network Remodeling. Mol Cell 2015;60(2):307–18 doi 10.1016/j.molcel.2015.09.002. [PubMed: 26455392]
25. Roadmap Epigenomics C, Kundaje A, Meuleman W, Ernst J, Bilenky M, Yen A, et al. Integrative analysis of 111 reference human epigenomes. Nature 2015;518(7539):317–30 doi 10.1038/nature14248. [PubMed: 25693563]
26. Suva ML, Rheinbay E, Gillespie SM, Patel AP, Wakimoto H, Rabkin SD, et al. Reconstructing and reprogramming the tumor-propagating potential of glioblastoma stem-like cells. Cell 2014;157(3):580–94 doi 10.1016/j.cell.2014.02.030. [PubMed: 24726434]
27. Darmanis S, Sloan SA, Croote D, Mignardi M, Chernikova S, Samghababi P, et al. Single-Cell RNA-Seq Analysis of Infiltrating Neoplastic Cells at the Migrating Front of Human Glioblastoma. Cell Rep 2017;21(5):1399–410 doi 10.1016/j.celrep.2017.10.030. [PubMed: 29091775]
28. Visel A, Rubin EM, Pennacchio LA. Genomic views of distant-acting enhancers. Nature 2009;461(7261):199–205 doi 10.1038/nature08451. [PubMed: 19741700]
29. Chapuy B, McKeown MR, Lin CY, Monti S, Roemer MG, Qi J, et al. Discovery and characterization of super-enhancer-associated dependencies in diffuse large B cell lymphoma. Cancer Cell 2013;24(6):777–90 doi 10.1016/j.ccr.2013.11.003. [PubMed: 24332044]
30. Loven J, Hoke HA, Lin CY, Lau A, Orlando DA, Vakoc CR, et al. Selective inhibition of tumor oncogenes by disruption of super-enhancers. Cell 2013;153(2):320–34 doi 10.1016/j.cell.2013.03.036. [PubMed: 23582323]
31. Pollen AA, Nowakowski TJ, Chen J, Retallack H, Sandoval-Espinosa C, Nicholas CR, et al. Molecular identity of human outer radial glia during cortical development. Cell 2015;163(1):55–67 doi 10.1016/j.cell.2015.09.004. [PubMed: 26406371]
32. Endres NF, Das R, Smith AW, Arkhipov A, Kovacs E, Huang Y, et al. Conformational coupling across the plasma membrane in activation of the EGF receptor. Cell 2013;152(3):543–56 doi 10.1016/j.cell.2012.12.032. [PubMed: 23374349]
33. Arkhipov A, Shan Y, Das R, Endres NF, Eastwood MP, Wemmer DE, et al. Architecture and membrane interactions of the EGF receptor. Cell 2013;152(3):557–69 doi 10.1016/j.cell.2012.12.030. [PubMed: 23374350]

34. Reznik E, Luna A, Aksoy BA, Liu EM, La K, Ostrovnaya I, et al. A Landscape of Metabolic Variation across Tumor Types. Cell Syst 2018;6(3):301–13 e3 doi 10.1016/j.cels.2017.12.014. [PubMed: 29396322]
35. Obukowicz MG, Welsch DJ, Salsgiver WJ, Martin-Berger CL, Chinn KS, Duffin KL, et al. Novel, selective delta6 or delta5 fatty acid desaturase inhibitors as antiinflammatory agents in mice. The Journal of pharmacology and experimental therapeutics 1998;287(1):157–66. [PubMed: 9765335]
36. Harmon SD, Kaduce TL, Manuel TD, Spector AA. Effect of the delta6-desaturase inhibitor SC-26196 on PUFA metabolism in human cells. Lipids 2003;38(4):469–76. [PubMed: 12848296]
37. Wang J, Liang H, Sun M, Zhang L, Xu H, Liu W, et al. Delta-6-desaturase inhibitor enhances radiation therapy in glioblastoma in vitro and in vivo. Cancer Manag Res 2018;10:6779–90 doi 10.2147/CMAR.S185601. [PubMed: 30584371]
38. Rees MG, Seashore-Ludlow B, Cheah JH, Adams DJ, Price EV, Gill S, et al. Correlating chemical sensitivity and basal gene expression reveals mechanism of action. Nature chemical biology 2016;12(2):109–16 doi 10.1038/nchembio.1986. [PubMed: 26656090]
39. Basu A, Bodycombe NE, Cheah JH, Price EV, Liu K, Schaefer GI, et al. An interactive resource to identify cancer genetic and lineage dependencies targeted by small molecules. Cell 2013;154(5): 1151–61 doi 10.1016/j.cell.2013.08.003. [PubMed: 23993102]
40. Mansour MR, Abraham BJ, Anders L, Berezovskaya A, Gutierrez A, Durbin AD, et al. Oncogene regulation. An oncogenic super-enhancer formed through somatic mutation of a noncoding intergenic element. Science 2014;346(6215):1373–7 doi 10.1126/science.1259037. [PubMed: 25394790]
41. Northcott PA, Lee C, Zichner T, Stutz AM, Erkek S, Kawauchi D, et al. Enhancer hijacking activates GFI1 family oncogenes in medulloblastoma. Nature 2014;511(7510):428–34 doi 10.1038/nature13379. [PubMed: 25043047]
42. Rohrig F, Schulze A. The multifaceted roles of fatty acid synthesis in cancer. Nature reviews Cancer 2016;16(11):732–49 doi 10.1038/nrc.2016.89. [PubMed: 27658529]
43. Tao BB, He H, Shi XH, Wang CL, Li WQ, Li B, et al. Up-regulation of USP2a and FASN in gliomas correlates strongly with glioma grade. J Clin Neurosci 2013;20(5):717–20 doi 10.1016/j.jocn.2012.03.050. [PubMed: 23416128]
44. Medes G, Thomas A, Weinhouse S. Metabolism of neoplastic tissue. IV. A study of lipid synthesis in neoplastic tissue slices in vitro. Cancer research 1953;13(1):27–9. [PubMed: 13032945]
45. Ookhtens M, Kannan R, Lyon I, Baker N. Liver and adipose tissue contributions to newly formed fatty acids in an ascites tumor. Am J Physiol 1984;247(1 Pt 2):R146–53 doi 10.1152/ajpregu.1984.247.1.R146. [PubMed: 6742224]
46. Mashimo T, Pichumani K, Vemireddy V, Hatanpaa KJ, Singh DK, Sirasanagandla S, et al. Acetate is a bioenergetic substrate for human glioblastoma and brain metastases. Cell 2014;159(7):1603–14 doi 10.1016/j.cell.2014.11.025. [PubMed: 25525878]
47. Srivastava NK, Pradhan S, Gowda GA, Kumar R. In vitro, high-resolution 1H and 31P NMR based analysis of the lipid components in the tissue, serum, and CSF of the patients with primary brain tumors: one possible diagnostic view. NMR in biomedicine 2010;23(2):113–22 doi 10.1002/nbm.1427. [PubMed: 19774696]
48. Li J, Condello S, Thomes-Pepin J, Ma X, Xia Y, Hurley TD, et al. Lipid Desaturation Is a Metabolic Marker and Therapeutic Target of Ovarian Cancer Stem Cells. Cell Stem Cell 2017;20(3):303–14 e5 doi 10.1016/j.stem.2016.11.004. [PubMed: 28041894]
49. Kim S, Jing K, Shin S, Jeong S, Han SH, Oh H, et al. omega3-polyunsaturated fatty acids induce cell death through apoptosis and autophagy in glioblastoma cells: In vitro and in vivo. Oncol Rep 2018;39(1):239–46 doi 10.3892/or.2017.6101. [PubMed: 29192322]
50. Guri Y, Colombi M, Dazert E, Hindupur SK, Roszik J, Moes S, et al. mTORC2 Promotes Tumorigenesis via Lipid Synthesis. Cancer Cell 2017;32(6):807–23 e12 doi 10.1016/j.ccell.2017.11.011. [PubMed: 29232555]
51. Buchanan FG, Wang D, Bargiacchi F, DuBois RN. Prostaglandin E2 regulates cell migration via the intracellular activation of the epidermal growth factor receptor. J Biol Chem 2003;278(37): 35451–7 doi 10.1074/jbc.M302474200. [PubMed: 12824187]

52. Tong WG, Ding XZ, Talamonti MS, Bell RH, Adrian TE. LTB4 stimulates growth of human pancreatic cancer cells via MAPK and PI-3 kinase pathways. Biochem Biophys Res Commun 2005;335(3):949–56 doi 10.1016/j.bbrc.2005.07.166. [PubMed: 16105664]

53. Ali A, Levantini E, Teo JT, Goggi J, Clohessy JG, Wu CS, et al. Fatty acid synthase mediates EGFR palmitoylation in EGFR mutated non-small cell lung cancer. EMBO Mol Med 2018;10(3) doi 10.15252/emmm.201708313.

54. Tang Z, Li C, Kang B, Gao G, Li C, Zhang Z. GEPIA: a web server for cancer and normal gene expression profiling and interactive analyses. Nucleic Acids Res 2017;45(W1):W98–W102 doi 10.1093/nar/gkx247. [PubMed: 28407145]

55. Yadav B, Wennerberg K, Aittokallio T, Tang J. Searching for Drug Synergy in Complex Dose-Response Landscapes Using an Interaction Potency Model. Comput Struct Biotechnol J 2015;13:504–13 doi 10.1016/j.csbj.2015.09.001. [PubMed: 26949479]

STATEMENT OF SIGNIFICANCE

Glioblastoma remains a devastating disease despite extensive characterization. We profiled epigenomic landscapes of glioblastoma to pinpoint cell-state-specific dependencies and therapeutic vulnerabilities. GSCs utilize polyunsaturated fatty acid synthesis to support membrane architecture, inhibition of which impairs EGFR signaling and GSC proliferation. Combinatorial targeting of these networks represents a promising therapeutic strategy.

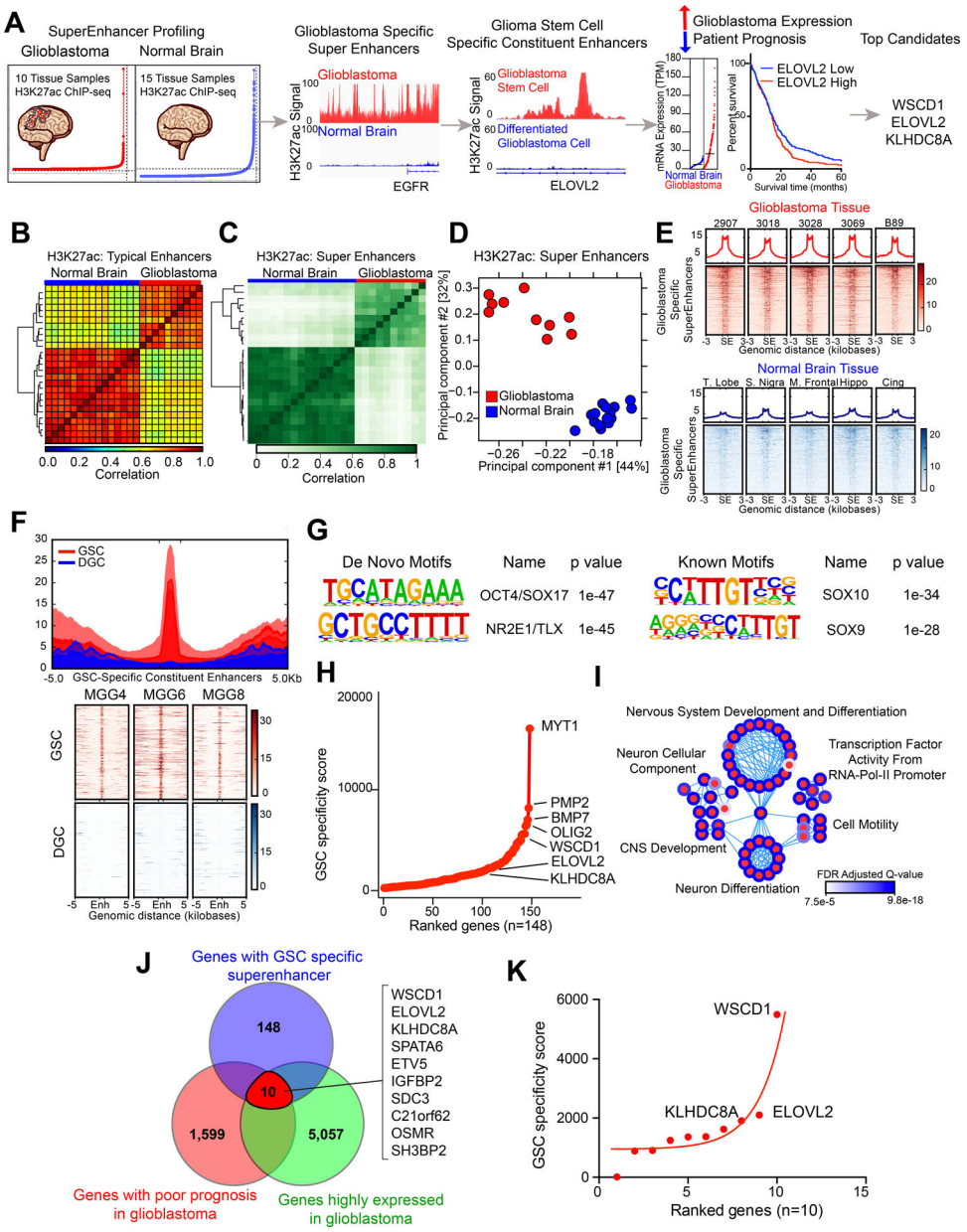

Figure 1. ***In silico*** **super-enhancer screen identifies potential glioblastoma stem cell specific therapeutic targets. See also Figure S1.**

(A) Diagram depicting the target selection strategy for the *in silico* super-enhancer screen.

(B) Clustering of 10 glioblastoma tissue samples and 15 normal brain tissue samples based on H3K27ac signal at typical enhancer regions. Color indicates the degree of Spearman correlation between individual samples.

(c) Clustering of 10 glioblastoma tissue samples and 15 normal brain tissue samples based on H3K27ac signal at super-enhancer regions defined by ROSE. Color indicates the degree of Pearson correlation between individual samples.

(d) Principal component analysis of 10 glioblastoma tissue samples and 15 normal brain tissue samples based on H3K27ac signal at super-enhancer regions defined by ROSE.

(E) H3K27ac signal over all glioblastoma-specific super-enhancers in glioblastoma tissue (upper portion, red) and normal brain tissue (lower portion, blue). Super-enhancer regions are scaled over a window 3 kilobases upstream and downstream of the super-enhancer.
(F) H3K27ac signal over all glioblastoma stem cell specific constituent enhancers in three matched glioblastoma stem cells (GSC) and differentiated glioblastoma cells (DGC) (MGG4, MGG6, and MGG8). The regions were defined by selecting all enhancers within glioblastoma specific super-enhancers as defined in (E) that were present in GSCs but absent in DGCs. GSC and DGC data was derived from (26).
(G) HOMER *de novo* and known motif enrichment analysis of GSC-specific enhancer constituents of glioblastoma-specific super-enhancers, as defined in (F).
(H) Hockey stick plot showing GSC specific super-enhancer associated genes ranked by "GSC specificity score," which depended on (1) number of gained H3K27ac peaks in GSC compared to DGC within the glioblastoma specific super-enhancer and (2) the fold change mRNA difference between GSCs and DGCs for the selected gene.
(I) Pathway enrichment bubble plot shows gene sets enriched among GSC specific super-enhancer associated genes, as described in (H).
(J) Venn diagram showing the intersection between genes for which high expression is associated with poor patient prognosis as calculated by the Cox proportional hazard test and the Log-rank test.
(K) Super-enhancer screen targets ranked by GSC-specificity score.

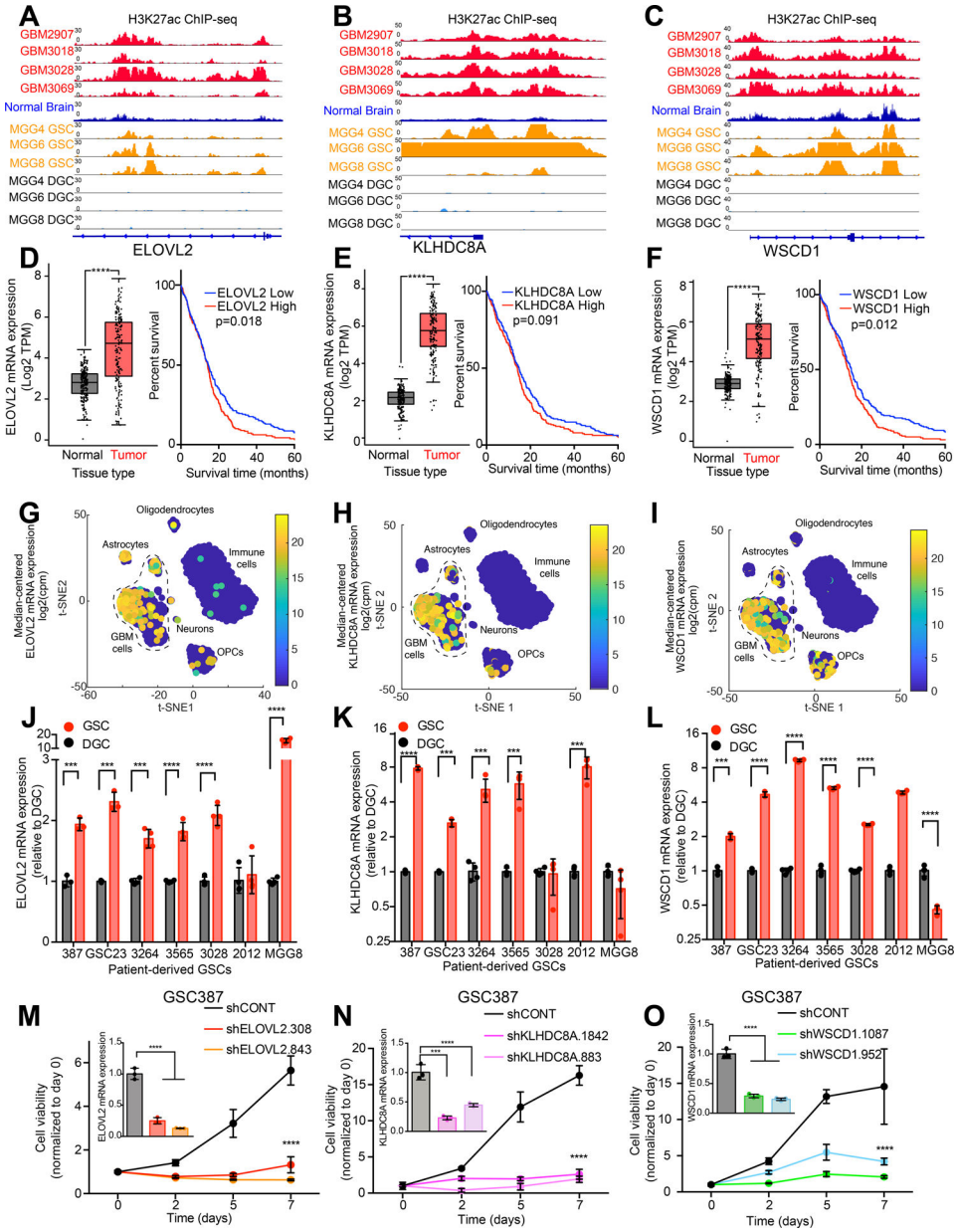

Figure 2. Glioblastoma stem cell specific super-enhancer target genes are critical for glioblastoma stem cell growth. See also Figure S2.

(A) H3K27ac signal at the ELOVL2 locus in glioblastoma primary tissue samples (GBM2907, GBM3018, GBM3028, and GBM3069), an overlay of 15 normal brain samples, and three GSC with matched DGC samples (MGG4, MGG6, and MGG8). GSC and DGC data were derived from (26).

(B) Same as (A) for KLHDC8A locus.

(C) Same as (A) for WSCD1 locus.

(D) (Left) mRNA expression Transcript Per Million (TPM) values in normal brain (GTEx, n=207) and glioblastoma (TCGA, n=163) from RNA-seq data for ELOVL2. Data was derived from (54). (Right) Kaplan-Meier curve showing survival of patients in the TCGA HG-U133A glioblastoma dataset stratified based on mRNA expression of ELOVL2. Cox

proportional hazard test (p=0.006) and log-rank analysis (p=0.018, “ELOVL2 low” n=268, “ELOVL2 high” n=257).

(E) Same as (D) for KLHDC8A. (Left) p=8.76e-82. (Right) Cox proportional hazard test (p=0.033), log-rank analysis (p=0.091, “KLHDC8A low” n=249, “KLHDC8A high” n = 276).

(F) Same as (D) for WSCD1. (Left) p=8.74e-42. (Right) Cox proportional hazard test (p=0.082), log-rank analysis (p=0.012, “WSCD1 low” n=243, “WSCD1 high” n = 282).

(G) Single-cell RNA-sequencing (scRNA-seq) data from glioblastoma specimens derived from (27) presented as a t-Distributed Stochastic Neighbor Embedding (t-SNE) plot demonstrating expression of ELOVL2 across glioblastoma cells, astrocytes, neurons, oligodendrocyte precursor cells (OPCs), and immune cells. Data is presented as median centered mRNA expression in counts per million (CPM).

(H) Same as (G) for KLHDC8A.

(I) Same as (G) for WSCD1.

(J) qPCR analysis of mRNA expression of ELOVL2 in 7 matched GSCs and DGCs with 4 technical replicates per condition. Student t-test with Holm-Sidak multiple test correction. ***, p<0.001. ****, p<0.0001.

(K) Same as (G) for KLHDC8A.

(L) Same as (G) for WSCD1.

(M) Cell viability in the GSC387 cell model over a 7-day time course following knockdown with two independent, non-overlapping shRNAs targeting ELOVL2 (shELOVL2.308, shELOVL2.843) or a non-targeting shRNA (shCONT). 5 technical replicates were performed for each group. Two-way repeated measures ANOVA with Dunnett’s multiple hypothesis test correction (****, p<0.0001). Inset shows qPCR analysis of mRNA expression of ELOVL2 following shRNA mediated knockdown. One-way ANOVA was used for statistical analysis with Dunnett’s multiple hypothesis test correction with three technical replicates. ****, p < 0.0001.

(N) Cell viability in the GSC387 cell model over a 7-day time course following knockdown with two independent, non-overlapping shRNAs targeting KLHDC8A (shKLHDC8A.1842, shKLHDC8A.883) or a non-targeting shRNA (shCONT). 5 technical replicates were performed for each group. Two-way repeated measures ANOVA with Dunnett’s multiple hypothesis test correction (****, p<0.0001). Inset shows qPCR analysis of mRNA expression of KLHDC8A following shRNA mediated knockdown. One-way ANOVA was used for statistical analysis with Dunnett’s multiple hypothesis test correction with three technical replicates. *** , p < 0.001, ****, p < 0.0001..

(O) Cell viability in the GSC387 cell model over a 7-day time course following knockdown with two independent, non-overlapping shRNAs targeting WSCD1 (shWSCD1.1087, shWSCD1.952) or a non-targeting shRNA (shCONT). 5 technical replicates were performed for each group. Two-way repeated measures ANOVA with Dunnett’s multiple hypothesis test correction (****, p<0.0001). Inset shows qPCR analysis of mRNA expression of WSCD1 following shRNA mediated knockdown. One-way ANOVA was used for statistical analysis with Dunnett’s multiple hypothesis test correction with three technical replicates. ****, p < 0.0001.

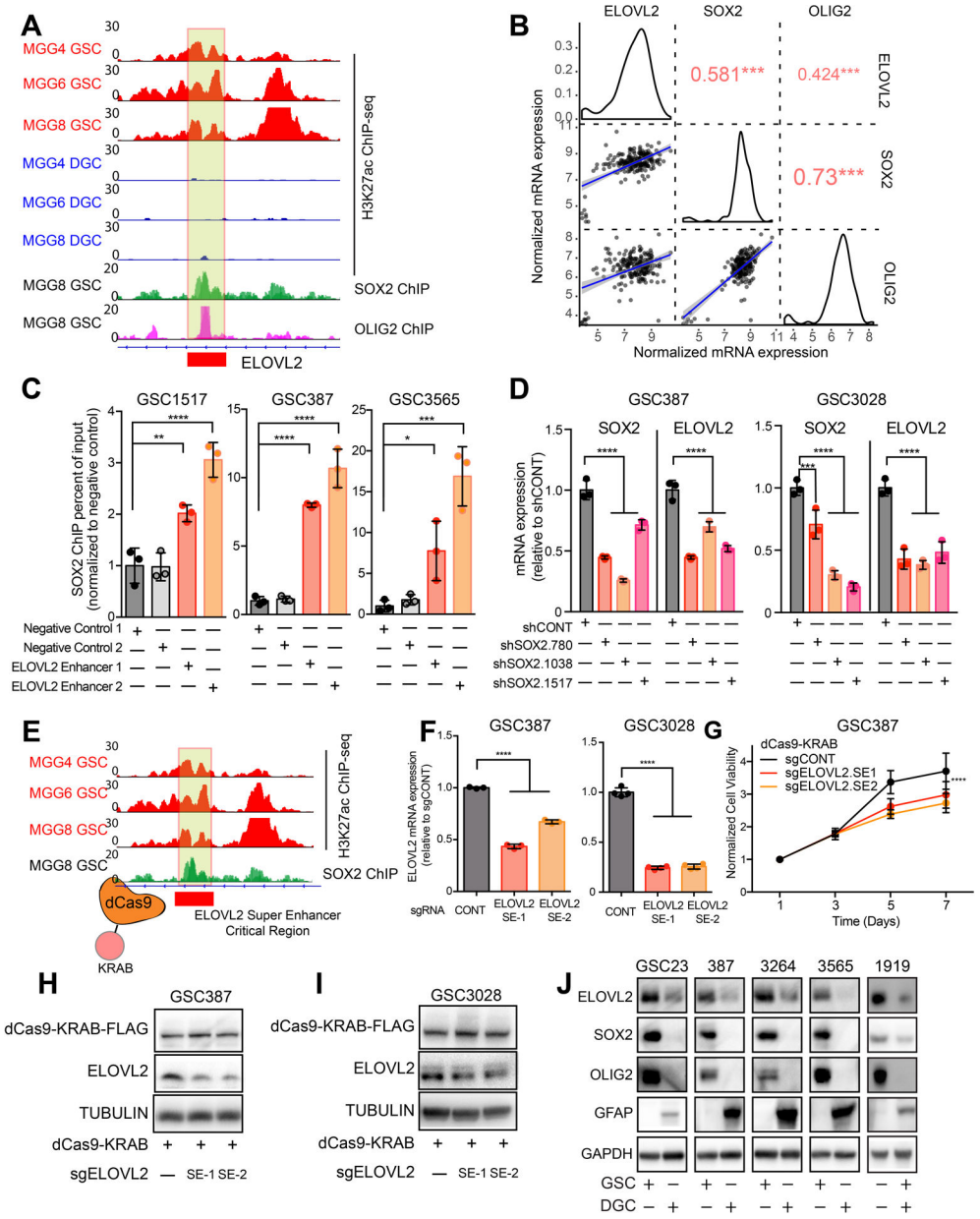

Figure 3. The ELOVL2 glioblastoma stem cell super-enhancer is driven by SOX2 and is necessary for maintenance of high ELOVL2 expression.

(A) H3K27ac signal at the ELOVL2 super-enhancer locus in three matched GSCs and DGCs (MGG4, MGG6, and MGG8). SOX2 and OLIG2 ChIP-seq data is shown at the same locus in the MGG8 model. Box indicates putative super-enhancer critical region with SOX2 binding site. Data was derived from (26).

(B) Correlation between ELOVL2, SOX2, and OLIG2 in the TCGA HG-U133A glioblastoma dataset restricted to the classical subtype. Red numbers indicate the correlation R value, *** $p < 0.001$.

(C) Enrichment of SOX2 binding over input by ChIP-qPCR in two negative control regions compared with two primers against the ELOVL2 super-enhancer region as demonstrated in (A). Three technical replicates were used for each condition. Statistical significance was

assessed using an ordinary one-way ANOVA with Dunnett multiple test correction. *, $p < 0.05$; **, $p < 0.01$; ***, $p < 0.001$; ****, $p < 0.0001$.

(D) qPCR analysis of mRNA expression of SOX2 and ELOVL2 following knockdown with three independent, non-overlapping shRNAs targeting SOX2 (shSOX2.780, shSOX2.1038, shSOX2.1517) or a non-targeting shRNA (shCONT). Three technical replicates were used for each condition. Statistical significance was assessed using a two-way ANOVA with Sidak multiple test correction, ****, $p < 0.0001$.

(E) Schematic showing targeting of the ELOVL2 Super-enhancer critical region using a catalytically-dead dCas9 fused to a transcriptional repressor domain (KRAB).

(F) qPCR analysis of ELOVL2 mRNA expression in GSC387 and GSC3028 cells following treatment with dCas9-KRAB and two sgRNAs targeting the ELOVL2 super-enhancer critical region or an empty dCas9-KRAB vector. Three technical replicates were used for each condition. One-way ANOVA with Dunnett's multiple comparison test, ****, $p < 0.0001$.

(G) Cell viability in the GSC387 cell model over a 7-day time course following treatment with dCas9-KRAB and two sgRNAs targeting the ELOVL2 super-enhancer critical region or an empty dCas9-KRAB vector. 6 technical replicates were performed for each group. Two-way repeated measures ANOVA with Dunnett's multiple hypothesis test correction (****, $p < 0.0001$).

(H) Western blot of ELOVL2 protein levels in GSC387 cells following treatment with dCas9-KRAB and two sgRNAs targeting the ELOVL2 super-enhancer critical region or an empty dCas9-KRAB vector. FLAG antibody was used to detect presence of the dCas9 protein.

(I) Same as (H) for GSC3028 cells.

(J) Western blot analysis of ELOVL2 protein levels in five GSCs and matched DGCs. SOX2 and OLIG2 were used to mark GSCs, while GFAP marked DGCs. GAPDH was used as a loading control.

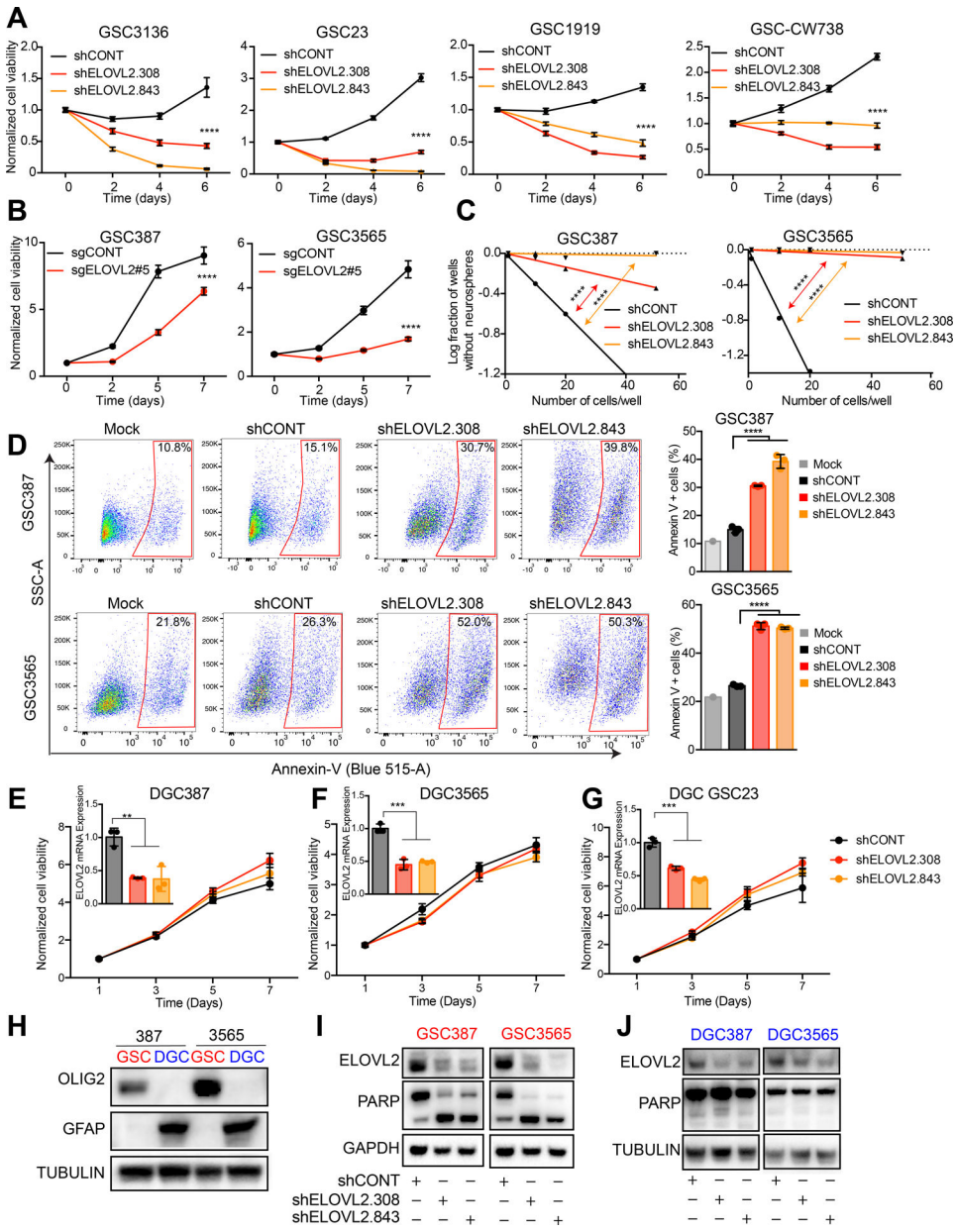

Figure 4. ELOVL2 knockdown impairs glioblastoma stem cell proliferation and self-renewal and induces apoptosis. See also Figure S3 and S4.

(A) Cell viability in the GSC3136, GSC23, GSC1919, and GSC-CW738 cells over a 6-day time course following knockdown with two independent, non-overlapping shRNAs targeting ELOVL2 (shELOVL2.308, shELOVL2.843) or a non-targeting shRNA (shCONT). 5 technical replicates were used for each condition. Two-way repeated measures ANOVA with Dunnett's multiple hypothesis test correction (****, $p < 0.0001$).

(B) Cell viability in the GSC387 and GSC3565 cells over a 7-day time course following CRISPR-Cas9 mediated ELOVL2 knockout or treatment with a non-targeting sgRNA. 7 technical replicates were used for each condition. Two-way repeated measures ANOVA was used for statistical analysis with Dunnett's multiple hypothesis test correction (****, $p < 0.0001$).

(C) *In vitro* limiting dilution assay in GSC387 and GSC3565 following knockdown with two independent, non-overlapping shRNAs targeting ELOVL2 or a non-targeting shRNA (shCONT). 20 wells were quantified for each condition. GSC387: shCONT vs shELOVL2.308, p = 7.51e-9. shCONT vs shELOVL2.843, p = 1.43e-19. GSC3565: shCONT vs shELOVL2.308, p = 4.7e-36. shCONT vs shELOVL2.843, p = 1.18e-41.
(D) Annexin-V staining of GSC387 and GSC3565 following knockdown with two independent, non-overlapping shRNAs targeting ELOVL2 or a non-targeting shRNA (shCONT). Three technical replicates were used for each condition. Quantification of Annexin-V staining using one-way ANOVA with Holm-Sidak multiple comparison test, **** $p < 0.0001$.
(E) Cell viability in the DGC387 cell model over a 7-day time course following knockdown with two independent, non-overlapping shRNAs targeting ELOVL2 (shELOVL2.308, shELOVL2.843) or a non-targeting shRNA (shCONT). 6 technical replicates were performed for each group. Inset shows qPCR analysis of mRNA expression of ELOVL2 following shRNA mediated knockdown. One-way ANOVA was used for statistical analysis with Dunnett's multiple hypothesis test correction with three technical replicates. **, $p < 0.01$.
(F) Cell viability in the DGC3565 cell model over a 7-day time course following knockdown with two independent, non-overlapping shRNAs targeting ELOVL2 (shELOVL2.308, shELOVL2.843) or a non-targeting shRNA (shCONT). 6 technical replicates were performed for each group. Inset shows qPCR analysis of mRNA expression of ELOVL2 following shRNA mediated knockdown. One-way ANOVA was used for statistical analysis with Dunnett's multiple hypothesis test correction with three technical replicates. ***, $p < 0.001$.
(G) Cell viability in the DGC GSC23 cell model over a 7-day time course following knockdown with two independent, non-overlapping shRNAs targeting ELOVL2 (shELOVL2.308, shELOVL2.843) or a non-targeting shRNA (shCONT). 6 technical replicates were performed for each group. Inset shows qPCR analysis of mRNA expression of ELOVL2 following shRNA mediated knockdown. One-way ANOVA was used for statistical analysis with Dunnett's multiple hypothesis test correction with three technical replicates. ***, $p < 0.001$.
(H) Western blot of GSC387, DGC387, GSC3565, and DGC3565. OLIG2 is used as a stem marker, GFAP is a differentiation marker, TUBULIN is a loading control.
(I) Western blot of GSC387 and GSC3565 following knockdown with two independent, non-overlapping shRNAs targeting ELOVL2 or a non-targeting shRNA (shCONT). GAPDH is used as a loading control.
(J) Western blot of DGC387 and DGC3565 following knockdown with two independent, non-overlapping shRNAs targeting ELOVL2 (shELOVL2.308, shELOVL2.843) or a non-targeting shRNA (shCONT). Tubulin is used as a loading control.

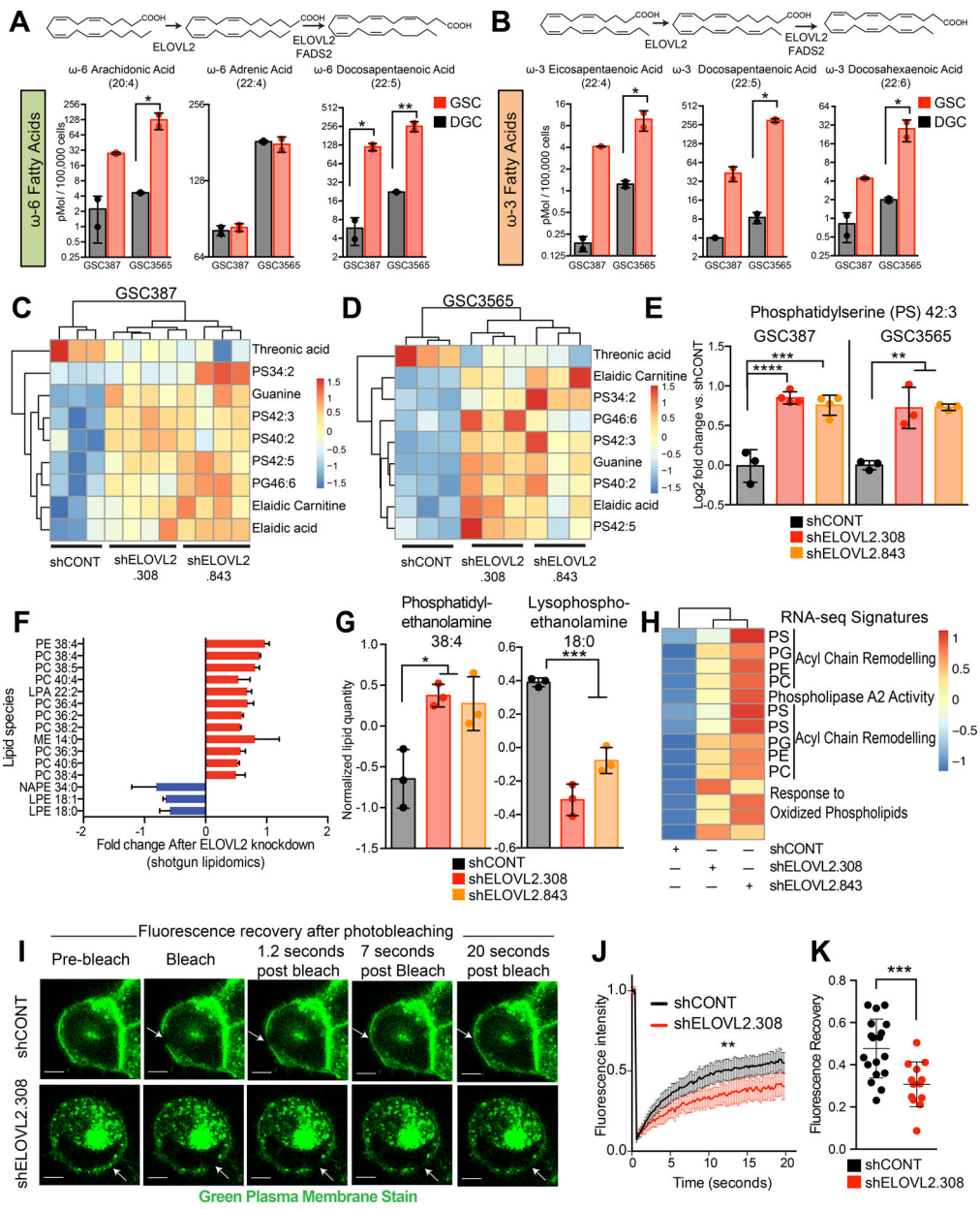

Figure 5. Glioblastoma stem cells utilize polyunsaturated fatty acid synthesis to maintain membrane phospholipid composition and integrity. See also Figure S5.

(A) Mass spectrometry analysis of ω-6 polyunsaturated fatty acids in two paired GSCs and DGCs (GSC387 and GSC3565). Statistical analysis was performed using an ordinary one-way ANOVA with Sidak multiple test correction with two technical replicates. *, $p < 0.05$; **, $p < 0.01$.

(B) Mass spectrometry analysis of ω-3 polyunsaturated fatty acids in two paired GSCs and DGCs (GSC387 and GSC3565). Statistical analysis was performed using an ordinary one-way ANOVA with Sidak multiple test correction with two technical replicates. *, $p < 0.05$.

(C) Consistently altered metabolites following knockdown with two independent, non-overlapping shRNAs targeting ELOVL2 or a non-targeting shRNA (shCONT) through global metabolomic profiling of GSC387.

(D) Same as (C) in GSC3565.

(E) Example of a consistently differential metabolite (phosphatidylserine 42:3) following global metabolomic profiling of GSC387 and GSC3565. Ordinary one-way ANOVA with Dunnet multiple test correction with three technical replicates. GSC387, shCONT vs shELOVL2.308, **** $p < 0.0001$; shCONT vs shELOVL2.843, *** $p < 0.001$. GSC3565, shCONT vs both shELOVL2.308 and shELOVL2.843, ** $p < 0.01$.

(F) Significant differential metabolites following knockdown with two independent, non-overlapping shRNAs targeting ELOVL2 or a non-targeting shRNA (shCONT) as assessed by shotgun lipidomics. Data was mean centered and metabolites shown are differentially abundant in both shRNA conditions relative to shCONT.

(G) (Left) An example of a differential lipid (phosphatidylethanolamine 38:4) following shotgun lipidomic profiling of the GSC387 model. Three technical replicates were performed. *, shCONT vs shELOVL2.308, $p = 0.01$. shCONT vs shELOVL2.843, $p = 0.03$. (Right) An example of a differential lipid (lysophosphoethanolamine 18:0) following shotgun lipidomic profiling of the GSC387 model. ***, shCONT vs shELOVL2.308, $p = 0.0002$. shCONT vs shELOVL2.843, $p = 0.0006$.

(H) Heatmap displays differential transcriptional signatures derived from RNA-sequencing following knockdown with two independent, non-overlapping shRNAs targeting ELOVL2 or a non-targeting shRNA (shCONT).

(I) Fluorescence recovery after photobleaching (FRAP) images following treatment with a non-targeting shRNA (shCONT) and an shRNA targeting ELOVL2 (shELOVL2.308) in the GSC387 tumor model. Images are taken over a 20 second time course and arrows indicate location of photobleaching. Scalebar indicates 5 μm.

(J) Fluorescence recovery after photobleaching (FRAP) recovery curves following knockdown with an shRNA targeting ELOVL2 (shELOVL2.308) or a non-targeting shRNA (shCONT) in the GSC387 tumor model. shCONT: n=18. shELOVL2: n=13. Mean with 95% confidence interval are displayed. Two-way repeated-measures ANOVA; **, $p = 0.0035$.

(K) Quantification of total fluorescence recovery following photobleaching after knockdown with an shRNA targeting ELOVL2 (shELOVL2.308) or a non-targeting shRNA (shCONT) in the GSC387 tumor model. shCONT, n=18. shELOVL2.308, n=13. Two-tailed unpaired t-test, ***, $p = 0.009$.

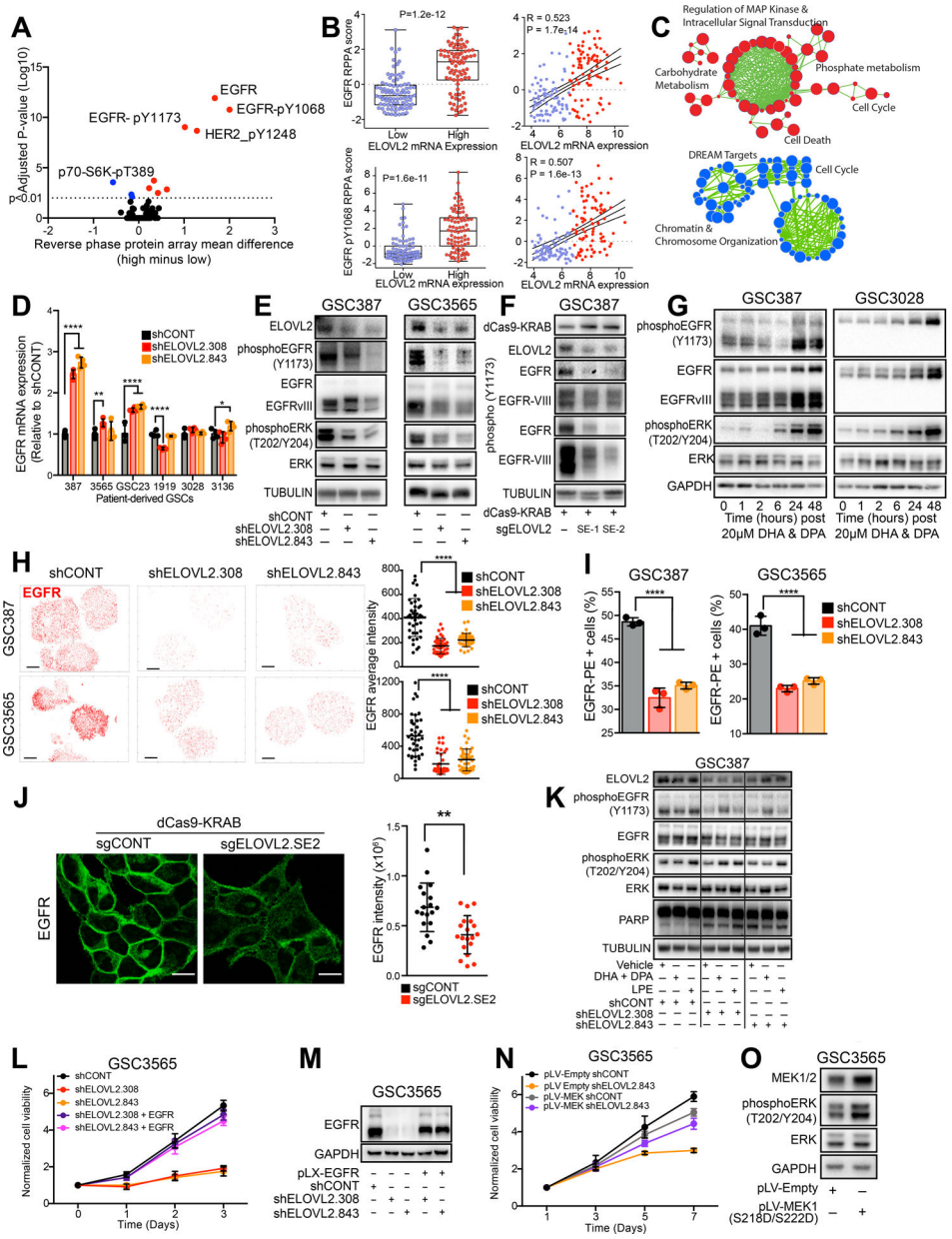

Figure 6. ELOVL2 is essential for maintaining efficient EGFR localization and signaling. See also Figure S6 and S7.

(A) Volcano plot demonstrating correlation between ELOVL2 mRNA expression in the TCGA HG-U133A microarray dataset with all proteins in the TCGA reverse phase protein array (RPPA) dataset from the glioblastoma cohort.

(B) Correlation between ELOVL2 mRNA expression in the TCGA HG-U133A microarray dataset with the TCGA reverse phase protein array (RPPA) dataset for EGFR and EGFR-pY1068. ELOVL2 low, n=88. ELOVL2 high, n=87.

(C) Pathway enrichment bubble plot shows gene sets enriched among genes that are significantly upregulated (red) or downregulated (blue) by RNA-sequencing following knockdown with two independent, non-overlapping shRNAs targeting ELOVL2 vs. a non-targeting shRNA (shCONT).

(D) qPCR analysis of EGFR mRNA expression in six glioblastoma stem cells (GSC387, GSC3565, GSC23, GSC1919, GSC3028, and GSC3136) following knockdown with two independent, non-overlapping shRNAs targeting ELOVL2 or a non-targeting shRNA (shCONT) with four technical replicates. Statistical significance was assessed using two-way ANOVA with Dunnett multiple test correction. *, $p < 0.05$; **, $p < 0.01$; ***, $p < 0.001$; ****, $p < 0.0001$.

(E) Western blot in GSC387 and GSC3565 following knockdown with two independent, non-overlapping shRNAs targeting ELOVL2 or a non-targeting shRNA (shCONT). Tubulin was used as a loading control.

(F) Western blot GSC387 cells following treatment with dCas9-KRAB and two sgRNAs targeting the ELOVL2 super-enhancer critical region or an empty dCas9-KRAB vector. FLAG antibody was used to detect presence of the dCas9 protein and TUBULIN is used as a loading control.

(G) Western blot in GSC387 and GSC3565 over a time course following treatment with 20 μM of ω-3 docosahexaenoic acid (DHA) and ω-6 docosapentaenoic acid (DPA). GAPDH was used as a loading control.

(H) Super-resolution stochastic optical reconstruction microscopy (STORM) imaging of EGFR following knockdown with two independent, non-overlapping shRNAs targeting ELOVL2 or a non-targeting shRNA (shCONT) in the GSC387 and GSC3565 model. Scale bars indicate 5 μm. (Right) Average EGFR intensity was quantified for individual cells and ordinary one-way ANOVA with Dunnett multiple test correction was used for statistical analysis. ****, $p < 0.0001$. GSC387: shCONT (n=40), shELOVL2.308 (n=42), shELOVL2.843 (n=40). GSC3565: shCONT (n=40), shELOVL2.308 (n=40), shELOVL2.843 (n=41).

(I) Flow cytometry analysis of cell surface EGFR following knockdown with two independent, non-overlapping shRNAs targeting ELOVL2 or a non-targeting shRNA (shCONT) in GSC387 and GSC3565 with three technical replicates. Ordinary one-way ANOVA with Dunnett multiple test correction was used for statistical analysis. ****, $p < 0.0001$.

(J) Immunofluorescence imaging of EGFR localization in GSC387 cells following treatment with dCas9-KRAB and an sgRNAs targeting the ELOVL2 super-enhancer critical region or an empty dCas9-KRAB vector. Images show optical slices. Scale bar indicates 10 μm. EGFR intensity was quantified for individual cells and a Mann-Whitney test was used for statistical analysis. **, $p = 0.0011$. sgCONT (n=18), sgELOVL2.SE2 (n=19).

(K) Western blot in GSC387 following knockdown with two independent, non-overlapping shRNAs targeting ELOVL2 or a non-targeting shRNA (shCONT). Cells were treated with vehicle, 20 μM of ω-3 docosahexaenoic acid (DHA) and ω-6 docosapentaenoic acid (DPA), or 50 μM of lysophosphatidylethanolamine (LPE). Tubulin was used as a loading control.

(L) Cell viability in the GSC3565 cell model over a 3-day time course following knockdown with two independent, non-overlapping shRNAs targeting ELOVL2 (shELOVL2.308, shELOVL2.843) or a non-targeting shRNA (shCONT) with or without over-expression of EGFR. 3 technical replicates were performed for each group.

(M) Western blot in the GSC3565 cell model following knockdown with two independent, non-overlapping shRNAs targeting ELOVL2 (shELOVL2.308, shELOVL2.843) or a non-targeting shRNA (shCONT) with or without over-expression of EGFR.

(N) Cell viability in the GSC3565 cell model over a 7-day time course following knockdown with an shRNAs targeting ELOVL2 (shELOVL2.843) or a non-targeting shRNA (shCONT) with or without over-expression of a constitutive active MEK (S218D, S222D). 6 technical replicates were performed for each group.

(O) Western blot in the GSC3565 cell model following over-expression of a constitutive active MEK (S218D, S222D).

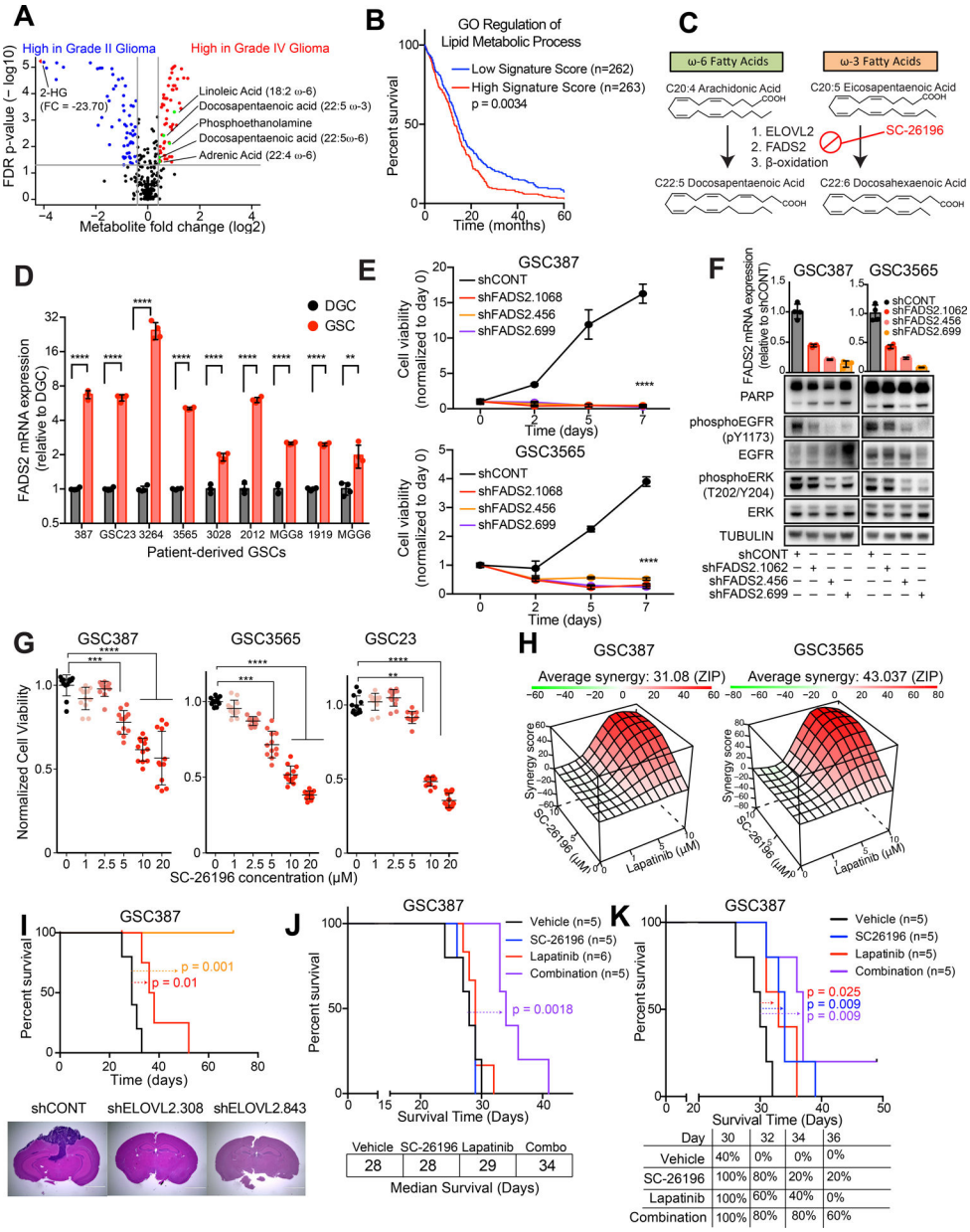

Figure 7. Polyunsaturated fatty acid synthesis is a clinical target for glioblastoma. See also Figure S8.

(A) Volcano plot showing differential metabolites between high grade glioma (grade IV) and low grade (grade II) glioma. Data was derived from (34).

(B) Kaplan-Meier curve showing survival of patients in the TCGA HG-U133A glioblastoma dataset stratified based on signature score from the “GO regulation of lipid metabolic process” signature. Log-rank analysis (p = 0.0034, “Signature low” n=262, “Signature high” n=263).

(C) Schematic showing metabolic pathways involved in ω-3 and ω-6 polyunsaturated fatty acid synthesis and mechanism of SC-26196.

(D) qPCR analysis of mRNA expression of ELOVL2 in 7 matched GSCs and DGCs with four technical replicates. Student t-test with Sidak multiple test correction, **, $p < 0.01$. ****, $p < 0.0001$.

(E) Cell viability in the GSC387 and GSC3565 cell model following knockdown with three independent, non-overlapping shRNAs targeting FADS2 (shFADS2.1062, shFADS2.456, shFADS2.699) or a non-targeting shRNA (shCONT). Two-way repeated measures ANOVA was used for statistical analysis with Dunnett's multiple hypothesis test correction with five technical replicates (****, $p < 0.0001$).

(F) FADS2 mRNA expression assessed by qPCR and EGFR signaling elements assessed by western blot following knockdown with three independent, non-overlapping shRNAs targeting FADS2 (shFADS2.1062, shFADS2.456, shFADS2.699) or a non-targeting shRNA (shCONT). Tubulin was used as a protein loading control.

(G) Cell viability in three GSCs was assessed following 6 days of treatment with SC-26196 at varying concentrations. Kruskal-Wallis test with Dunn's multiple comparisons test with four technical replicates and three biological replicates. **, $p < 0.01$,***, $p < 0.001$. ****, $p < 0.0001$.

(H) In vitro synergy diagram of combinatorial lapatinib and SC-26196 treatment following combinatorial treatment with lapatinib (0,1,5,10 μM) and SC-26196 (0,5,10 μM). Cell viability was assessed after 3 days of treatment. ZIP score was used to assess synergy (55).

(I) (Top) Kaplan-Meier curve showing survival of mice following implantation with GSC387 following knockdown with two independent, non-overlapping shRNAs targeting ELOVL2 or a non-targeting shRNA (shCONT). n=5 mice per arm. shCONT vs. shELOVL2.308, $p = 0.01$. shCONT vs. shELOVL2.843, $p = 0.001$. (Bottom) Hematoxylin and eosin staining of brains following implantation with GSC387 following shCONT or shELOVL2 treatment.

(J) Kaplan-Meier curve showing survival of mice following implantation with GSC387 following treatment with vehicle control, SC-26196 (10μM), lapatinib (5μM), or a combination (10 μM SC-26196 + 5 μM lapatinib) *in vitro*. n=5 mice for vehicle, SC26196, and combination arms. n=6 for lapatinib arm. Log-rank, $p = 0.0018$.

(K) Kaplan-Meier curve showing survival of mice following implantation with GSC387 and treatment with vehicle, 125 mg/kg of SC-26196, 30 mg/kg of lapatinib, or a combination (125 mg/kg of SC-26196 and 30 mg/kg of lapatinib). n=5 mice per arm. Log-rank test was used for statistical analysis. Vehicle vs. SC-26196 ($p = 0.009$). Vehicle vs. lapatinib ($p = 0.025$). Vehicle vs. combination ($p = 0.009$). SC-26196 vs. combination ($p = 0.27$). Lapatinib vs. combination ($p = 0.06$).